energies

MDPI

Article

Model Predictive Control of a Stand-Alone Hybrid Battery-Hydrogen Energy System: A Case Study of the PHOEBUS Energy System

Alexander Holtwerth [1,*], André Xhonneux [1] and Dirk Müller [1,2]

[1] Institute of Climate and Energy Systems, Energy Systems Engineering (ICE-1), Forschungszentrum Jülich GmbH, 52428 Jülich, Germany; a.xhonneux@fz-juelich.de (A.X.); dmueller@eonerc.rwthaachen.de (D.M.)
[2] E.ON Energy Research Center, Institute for Energy Efficient Buildings and Indoor Climate, RWTH Aachen University, 52056 Aachen, Germany
* Correspondence: a.holtwerth@fz-juelich.de

Abstract: Model predictive control is a promising approach to robustly control complex energy systems, such as hybrid battery-hydrogen energy storage systems that enable seasonal storage of renewable energies. However, deriving a mathematical model of the energy system suitable for model predictive control is difficult due to the unique characteristics of each energy system component. This work introduces mixed integer linear programming models to describe the nonlinear multidimensional operational behavior of components using piecewise linear functions. Furthermore, this paper develops a new approach for deriving a strategy for seasonal storage of renewable energies using cost factors in the objective function of the optimization problem while considering degradation effects. An experimentally validated simulation model of the PHOEBUS Energy System is utilized to compare the performance of two model predictive controllers with a hysteresis band controller such as utilized for the real-world system. Furthermore, the sensitivity of the model predictive controller to the prediction horizon length and the temporal resolution is investigated. The prediction horizon was found to have the highest impact on the performance of the model predictive controller. The best-performing model predictive controller with a 14-day prediction horizon and perfect foresight increased the total energy stored at the end of the year by 18.9% while decreasing the degradation of the electrolyzer and the fuel cell.

Keywords: model predictive control; optimization; mixed integer linear programming; hybrid battery-hydrogen energy storage system

check for updates

Citation: Holtwerth, A.; Xhonneux, A.; Müller, D. Model Predictive Control of a Stand-Alone Hybrid Battery-Hydrogen Energy System: A Case Study of the PHOEBUS Energy System. *Energies* **2024**, *17*, 4720. https://doi.org/10.3390/en17184720

Academic Editor: Ahmed Abu-Siada

Received: 21 August 2024
Revised: 16 September 2024
Accepted: 20 September 2024
Published: 22 September 2024

Copyright: © 2024 by the authors. Licensee MDPI, Basel, Switzerland. This article is an open access article distributed under the terms and conditions of the Creative Commons Attribution (CC BY) license (https://creativecommons.org/licenses/by/4.0/).

1. Introduction

To counteract climate change, large capacities of renewable energy sources (RESs), like photovoltaic (PV) systems, are installed to reduce the reliance on fossil energy sources [1]. However, due to the high volatility of RES, energy storage is needed to compensate for the underproduction of renewable energy during some parts of the year. This is especially true for stand-alone energy systems that need large energy storage systems to achieve complete grid independence [2].

The combination of hydrogen storage systems (HSSs) and battery storage systems (BSSs) in a hybrid battery-hydrogen storage system was shown to yield a cost-effective combination compared to hydrogen-only or battery-only energy storage systems if seasonal storage is considered [3]. Hybrid battery-hydrogen energy systems enable an all-year-long supply of renewable energies by utilizing the battery as an efficient short-term storage solution and the hydrogen energy storage system for long-term storage of energy [4]. The design aspects of hybrid battery-hydrogen energy storage systems are widely studied in literature [2,5–7]. The consideration of HSS becomes cost-effective if a high share of renewable energies is to be achieved by the energy storage system [8].

For an autonomous operation of a hybrid battery-hydrogen energy storage system, an energy management strategy (EMS) is needed for a continuous supply of power to the demand [9]. Furthermore, the EMS is crucial for the efficiency and longevity of an energy system [10,11]. Therefore, developing an EMS that considers efficiency and longevity is essential for a stand-alone energy system. However, deriving a suitable EMS is a non-trivial task.

Rule-based controllers (RBCs) are prevalent in practical applications, such as EMSs [12]. Rule-based controllers are utilized due to their simplicity and ease of implementation [13]. Modu et al. [14] utilized a rule-based EMS to manage the power flow between components in their metaheuristic optimization algorithm for the energy management and capacity planning of a stand-alone energy system. Similarly, Li et al. [15] utilized a hysteresis band controller (e.g., an EMS) in their multi-objective optimization approach to determine the optimal system configuration while considering degradation effects. Moreover, Alili et al. [16] utilized a rule-based controller in their techno-economic assessment of integrating HSS into a hybrid energy storage system with a pumped storage hydropower plant.

Another EMS used for controlling hybrid battery-hydrogen energy storage is model predictive control (MPC). MPC utilizes a mathematical model of the energy system in combination with a forecast of future external conditions to determine the optimal operational strategy using mathematical optimization [13]. Some historic and more recent examples of the utilization of MPC as EMSs can be found in [17–23]. Generally, MPC leads to more efficient utilization of hybrid battery-hydrogen energy storage systems than RBCs. Gonzalez-Rivera et al. [24] benchmarked their MPC approach against an RBC and found that MPC reduced the utilization cost by 25.3% for the investigated hybrid charging station. Furthermore, the MPC, derived by Yamashita et al. [25], reduced the annual costs up to 5% in residential buildings and 9% in non-residential buildings compared to an RBC. Recently, Thaler et al. [26] showed that by utilizing MPC in comparison to RBC, the system size of their hybrid battery-hydrogen energy storage system, and therefore, the costs could be decreased by 12%.

The mathematical model utilized for the optimization problem is essential for MPC. In the scope of hybrid battery-hydrogen energy systems, mixed integer linear programming (MILP) optimization problems are commonly derived to optimize the design or operation of the energy system [20,21,25–30]. However, one difficulty that arises from utilizing MILP optimization problems is the derivation of models for the nonlinear operational behavior of components such as the electrolyzer. One method commonly used in literature is the utilization of a constant nominal efficiency for the electrolyzer and fuel cell [21,22,31–33]. Another way to approximate the nonlinear operational behavior is using piecewise linear models [5,25,26]. Piecewise linear functions generally approximate the nonlinear behavior with higher accuracy than simple linear approximations [34], which can lead to reduced energy conversion losses for hybrid battery-hydrogen energy storage systems [35].

Most piecewise linear models in literature approximate the operational behavior using univariate functions. However, in practice, some component dynamics need to be modeled using multiple input variables, for instance, a temperature-variable electrolyzer, as described by Ulleberg [36]. Recently, some works have focused on deriving temperature-dependent models for hybrid energy storage systems. Huang et al. [30] considered a constant electrolyzer efficiency in their MILP model that is continuously updated in their plant model. Li et al. [37] considered linear models to approximate the temperature-dependent component behaviors in their optimization problem. Similarly, Khaligh et al. [38] linearized the operational behavior of their temperature-variable electrolyzer with a linear model for the power and heat output of the electrolyzer. Pan et al. [39] considered the temperature dynamics of the electrolyzer using a linear approximation while linearizing the operational behavior of the electrolyzer. However, multidimensional piecewise linear models can be derived using approaches from literature such as those presented by Kämper et al. [40] or Birkelbach et al. [34]. Thus, more detailed models of the multidimensional operational behavior can be derived.

This work shows an approach for modeling the multidimensional nonlinear operational behavior of hydrogen storage components with piecewise linear models using the data-driven modeling toolbox LinMOG [41,42] and the hinging hyperplane tree algorithm as explained by Kämper et al. [40]. Thus, a detailed MILP optimization problem is derived that directly approximates the multidimensional operational behavior of several components. The novelty of the MILP optimization models derived in this work compared to approaches found in the literature [30,37–39] is the derivation of multidimensional piecewise linear models that are combined to model the system dynamics directly. Thus, a novel MILP optimization problem is derived that enables the derivation of operational strategies that exploit the nonlinear multidimensional temperature dynamics of an electrolyzer, the nonlinear multidimensional voltage characteristics of a battery, and the nonlinear characteristics of a fuel cell to increase the energy efficiency of the hybrid battery-hydrogen energy storage system. Furthermore, a second optimization problem is derived, simplifying the operational behavior to compare the resulting performance of an MPC with the detailed and simplified optimization model.

Another challenge for MPC is adopting a long-term strategy for the energy storage system. The main challenge is incorporating the seasonal strategy into the short prediction horizon of an operational optimization [26]. Only a few studies have investigated the integration of a long-term strategy into the operation of a hybrid battery-hydrogen energy storage system. For instance, Thaler et al. [26] utilized an extra cost factor in the objective function to incentivize hydrogen storage. Wakui et al. [43] utilized a simplified long-term operational optimization problem to calculate a lower bound of the original problem. In the second step, the short-term planning is updated by a receding horizon approach. A similar approach was derived by Guo et al. [44], using a simplified optimization problem and historical data to derive a long-term operational strategy for a hybrid energy storage system. Furthermore, Guo et al. [44] propose a data-driven scheduling correction framework to update the reference state of charge for seasonal storage with newly observed data and, in the second step, to solve a bi-objective optimization problem to minimize the operational cost. However, solving a long-term operational optimization problem with a prediction horizon of one year requires significant simplifications in the optimization problem. Thus, this work adapts the approach of Thaler et al. [26] with a novel approach to incentivize energy storage. The main difference to the work of Thaler et al. [26] is that a single objective for the operational optimization problem is developed that incentivizes energy storage by calculating cost factors based on storage capacities. Moreover, this work considers multiple typical degradation effects for the fuel cell and the electrolyzer by adding additional terms to the objective function to reduce the component degradation while increasing the system efficiency.

Besides considering a long-term strategy, the prediction horizon of a scheduling optimization problem can be an impacting factor for the effectiveness of a model predictive controller. In the literature, a prediction horizon of 24 h or less is considered by many authors [18,19,31,32,45–47]. However, longer prediction horizons might increase the performance of an MPC. For instance, Cardona et al. [23] showed that utilizing a seven-day prediction horizon led to an increased performance of their model predictive controller for controlling a hydrogen production and refueling station. Furthermore, Holtwerth et al. [48] showed that increasing the prediction horizon for a grid-connected hybrid battery-hydrogen energy storage system can increase the performance of a model predictive controller. Thus, this work conducts a novel study on the impact of a long prediction horizon for a stand-alone hybrid battery-hydrogen energy storage system considering seasonal storage. Therefore, the prediction horizon is increased up to 14 days. Furthermore, the impact of the prediction horizon, the temporal resolution, and the modeling detail on the performance and the optimization run time of a model predictive controller is investigated. Thus, this work conducts an extensive study by simulating the system's operation over multiple years using multiple model predictive controllers.

The hybrid battery-hydrogen energy storage system of the PHOEBUS project [49] is utilized as a case study for the developed methods. The operation of the energy storage system was well studied in the literature [4,49–51] and investigated for more than ten years [52]. Furthermore, a detailed simulation model of the PHOEBUS Energy System was derived and experimentally validated by Ulleberg [4]. Thus, the simulation model of Ulleberg [4] can be utilized as a substitute for the real-world system to benchmark the different model predictive controllers. Furthermore, the potential of model predictive control for this energy storage system is shown by comparing the resulting operation of the energy storage system derived by a model predictive controller with two hysteresis band controllers (HBCs) such as those utilized for the real-world operation of the PHOEBUS Energy System [4].

In summary, this work addresses the challenge of deriving accurate MILP optimization models for the nonlinear multidimensional operational behavior of energy system components and the challenge of adopting a long-term strategy for energy storage. The performance of the derived MPC is benchmarked using an experimentally validated simulation model of the real-world energy storage system. The key contributions of this work are as follows:

- Development of novel piecewise-linear multidimensional MILP optimization models to enable the exploitation of the nonlinear multidimensional dynamics of the electrolyzer, the battery, and the fuel cell.
- Adaptation of the objective function to enable seasonal storage with a limited prediction horizon in the optimization problem.
- Extensive parameter study of the impact of the model accuracy, the temporal resolution, and the prediction horizon for a model predictive controller.

This work is structured as follows: Section 2 describes the simulation model of the PHOEBUS Energy System and the two optimization models used for MPC. Next, Section 3 describes the case study conducted in this work. Furthermore, Section 4 visualizes and discusses the results of the case study. Finally, Section 5 draws a conclusion.

2. Methods

In this work, two different models are implemented to represent the PHOEBUS Energy System. First, Section 2.1 shows the implementation of the simulation model based on the work of Ulleberg [4] that is used as a substitute for the real-world energy system. Second, in Sections 2.2 and 2.3, the MILP optimization models are explained that are developed in this work and utilized in the scope of the model predictive controller.

2.1. Simulation Model

The PHOEBUS Energy System was a hybrid battery-hydrogen energy storage system operated at the research center in Jülich between 1993 and around 2001. Multiple publications were published in the scope of the project describing various aspects of the energy system [4,36,49–52]. The energy system is visualized in Figure 1.

As shown in Figure 1, the energy system consists of an alkaline electrolyzer, a PEM fuel cell, a lead-acid battery, multiple PV systems, multiple DC/DC converters, and a DC/AC inverter to supply a grid-independent electricity demand. The hydrogen produced in the electrolyzer at a pressure of pr^{ey} = 7 bar is first stored in a low-pressure storage tank with a volume of $V^{ps,lp}$ = 25 m^3 and a maximal pressure of $pr^{ps,lp,max}$ = 7 bar. Next, the hydrogen is compressed to the pressure within the high-pressure storage tank with a volume of $V^{ps,hp}$ = 26.8 m^3 and a maximal pressure of $pr^{ps,hp,max}$ = 120 bar. All components except the compressor are connected to a DC busbar. The battery voltage determines the voltage of the DC busbar since the battery is directly coupled with the DC busbar [52]. The real-world system was controlled by setting the converter power of the fuel cell and the electrolyzer [50], while the battery is responsible for the grid balancing such that the energy balance for a given electricity output of the photovoltaic (PV) cells and a given electricity demand is always satisfied. The electrolyzer is an alkaline electrolyzer operated at a variable

temperature of up to $T^{ey,max}$ = 80 °C with a maximum power of $p^{ey,max}$ = 26 kW. The stack voltage of the electrolyzer was limited to $U^{ey,max}$= 40 V [4] while the minimal and maximal allowed currents were at $i^{ey,min}$ = 135 A and $i^{ey.max}$ = 750 A, respectively. The fuel cell considered in this work is a PEM-fuel cell as described by Ulleberg [4] with a maximal electricity output of $p^{fc,max}$ = 6 kW. Furthermore, the minimal and maximal allowed currents for the fuel cell operation were $i^{fc,min}$ = 20 A and $i^{fc,max}$ = 200 A. The battery had a capacity of around 303 kWh (at 10 A) [52] while the maximal charging and discharging current are assumed to be $i^{bat,ch/dc,max}$ = 80 A. Furthermore, the battery voltage was variable between values of U^{bat} = 200–260 V. An overview of the component sizes is given in Table 1.

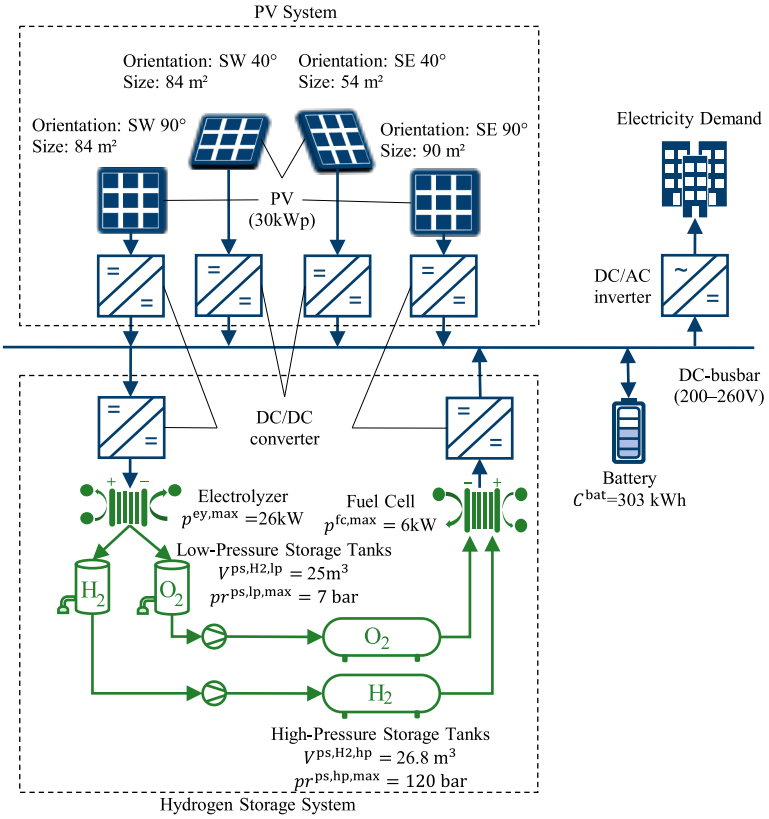


Figure 1. Sketch of the PHOEBUS Energy System. Figure based on [52].

Ulleberg [4] derived simulation models for all components of the PHOEBUS Energy System as well as for the whole system. These simulation models were derived from real-world operating data and were experimentally validated by Ulleberg [4]. A short description of the simulation models is given in the following, while an extensive explanation of the derivation of these models can be found in the work by Ulleberg [4].
Ulleberg [4] derived a bivariate polynomial to model the cell voltage of the electrolyzer $U^{ey,cell}$ as a function of the current i^{ey} and the stack temperature T^{ey}

$$U^{ey,cell} = f(i^{ey}, T^{ey}). \quad (1)$$

Furthermore, a polynomial was derived by Ulleberg to approximate the Faraday efficiency $\eta^{ey,far}$

$$\eta^{ey,far} = f(i^{ey}, T^{ey}). \quad (2)$$

The electricity consumption p^{ey} of the electrolyzer is calculated using the stack voltage U^{ey}, as follows:

$$U^{ey} = U^{ey,cell} \cdot n^{cell,ey} \quad (3)$$

where $n^{\text{cell,ey}}$ is the number of cells, and the current i^{ey} is given by the following:

$$p^{\text{ey}} = U^{\text{ey,st}} \cdot i^{\text{ey}}. \tag{4}$$

Finally, the hydrogen production is calculated by the following [4]:

$$\dot{n}^{\text{H2,ey}} = \eta^{\text{ey,far}} \frac{n^{\text{cell,ey}} \cdot i^{\text{ey}}}{2 \cdot F} \tag{5}$$

where F is the Faraday constant. Furthermore, the power input of the DC/DC converter is calculated using a bivariate polynomial, considering the stack voltage and the power input of the electrolyzer as variables, as follows:

$$p^{\text{ey,conv}} = f(U^{\text{ey}}, p^{\text{ey}}). \tag{6}$$

In the real-world system, the stack voltage was limited to $U^{\text{ey,max}}$ = 40 V such that the maximum current of $i^{\text{ey,max}}$ = 750 A could only be applied once the electrolyzer has reached a temperature of around T^{ey} = 330 K. The resulting operational behavior of the electrolyzer, its DC/DC converter, and the temperature-dependent efficiency curves are shown in Figure 2. A detailed mathematical description was conducted by Ulleberg in [4,36].

Table 1. Overview of component sizes of the PHOEBUS Energy System.

Component Name	Parameter	Value
Electrolyzer	$i^{\text{ey,max}}$	750 A
	$i^{\text{ey,min}}$	135 A
	$U^{\text{ey,max}}$	40 V
	$p^{\text{ey,max}}$	26 kW
	$T^{\text{ey,max}}$	80 °C
	pr^{ey}	7 bar
Fuel Cell	$i^{\text{fc,max}}$	200 A
	$i^{\text{fc,min}}$	20 A
	$p^{\text{fc,max}}$	6 kW
Battery	U^{bat}	200–260 V
	$i^{\text{bat,ch/dc,max}}$	80 A
	$c^{\text{bat,nom}}$	303 kWh
Pressure Storage	$V^{\text{ps,lp}}$	25 m^3
	$pr^{\text{ps,lp,max}}$	7 bar
	$V^{\text{ps,hp}}$	26.8 m^3
	$pr^{\text{ps,hp,max}}$	120 bar
PV	$p^{\text{PV,max}}$	30 kW
	E^{PV}	27.18 MWh
Demand	$p^{\text{ed,max}}$	13.73 kW
	E^{ed}	19.76 MWh

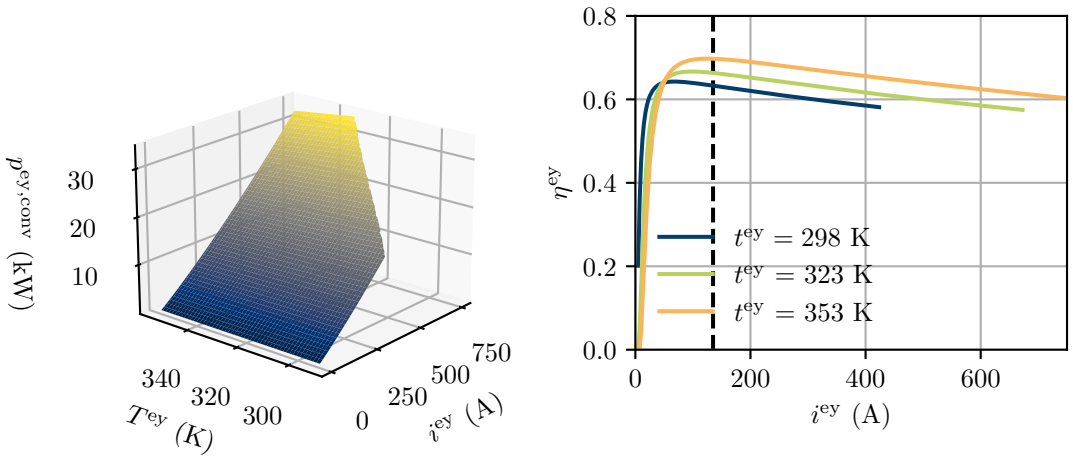
A temperature change of the electrolyzer is calculated depending on its operational mode. If the electrolyzer is turned on, waste heat is generated $\dot{Q}^{\text{gen,ey}}$, while at the same time heat losses due to natural cooling $\dot{Q}^{\text{loss,ey}}$ occur, and additional cooling $\dot{Q}^{\text{cool,ey}}$ with tab water is applied. Thus, a temperature change can be calculated as follows by assuming constant heat generation and losses for a short time interval Δt [4]:

$$T_{i+1}^{\text{ey}} = T_i^{\text{ey}} + \frac{\Delta t}{C^{\text{ey}}} (\dot{Q}^{\text{gen,ey}} - \dot{Q}^{\text{loss,ey}} - \dot{Q}^{\text{cool,ey}}), \tag{7}$$

where C^{ey} is the heat capacity of the electrolyzer. On the contrary, only natural cooling occurs if the electrolyzer is turned off:

$$T^{ey}_{i+1} = T^{ey}_{i} - \frac{\Delta t}{C^{ey}} \dot{Q}^{loss,ey} \tag{8}$$

A detailed description of the thermal model of the electrolyzer can be found in [4].



(**a**) Operational behavior (**b**) Efficiency

Figure 2. Operational behavior and efficiency curves of the temperature-variable electrolyzer. The dashed black line indicates the minimal allowed current $i^{ey,min}$.

The cell voltage of the fuel cell $U^{fc,cell}$ is modeled by Ulleberg [4] assuming a constant stack temperature and pressure

$$U^{fc,cell} = f(i^{fc}) \tag{9}$$

where i^{fc} is the current through the fuel cell. Furthermore, the hydrogen consumption $n^{H2,fc}$ is calculated assuming a constant Faraday efficiency $\eta^{fc,far}$, as follows:

$$\dot{n}^{fc} = \eta^{fc,far} \cdot \frac{n^{cell,fc} \cdot i^{fc}}{2 \cdot F} \tag{10}$$

where $n^{cell,fc}$ is the number of cells. Furthermore, the power output of the fuel cell p^{fc} is calculated by the following:

$$p^{fc} = i^{fc} \cdot n^{cell,fc} \cdot U^{fc,cell}. \tag{11}$$

The DC/DC converter of the fuel cell is modeled as a polynomial, and its efficiency depends on the voltage of the DC busbar and the output power of the fuel cell. Thus, the power output of the fuel cell system, including the converter at the DC busbar $p^{fc,conv}$, is a function of the power output of the fuel cell and the voltage of the DC busbar U^{bus}

$$p^{fc,conv} = f(U^{bus}, p^{fc}). \tag{12}$$

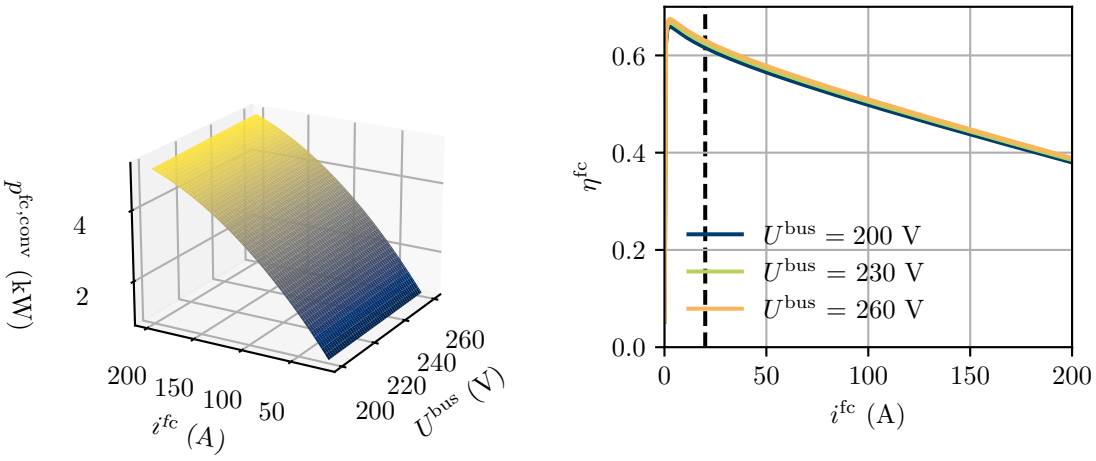
The operational behavior and efficiency of the fuel cell, including the DC/DC converter, are shown in Figure 3.

The model of the compressor is based on a two-stage polytropic compression process with inter-cooling, as described by Ulleberg [4]:

$$p^{comp} = \frac{n^{comp}}{\eta^{comp}} \left(w^{comp,1} + w^{comp,2} \right) \tag{13}$$

$$w^{comp,1/2} = \frac{n \cdot R \cdot T^{in}}{n-1} \left[1 - \left(\frac{pr^{out,1/2}}{pr^{in,1/2}} \right)^{\frac{n-1}{n}} \right] \tag{14}$$

where T^{in} is the inlet temperature, R is the universal gas constant, η^{comp} is the compressor efficiency, n is the polytropic coefficient, n^{comp} is the hydrogen flow through the compressor, and $pr^{\text{in},1/2}$ and $pr^{\text{out},1/2}$ are the inlet and outlet pressures of each compressor stage. The inlet pressure of the first stage $pr^{\text{in},1}$ is equal to the pressure of the low-pressure storage tank pr^{lp}, and the outlet pressure of the second stage $pr^{\text{out},2}$ is equal to the pressure of the high-pressure storage tank pr^{hp}.



(**a**) Operational behavior. (**b**) Efficiency

Figure 3. Operational behavior and efficiency curves of the fuel cell and its converter. The dashed black line indicates the minimal allowed current $i^{\text{fc,min}}$.

The pressure within both pressure storage tanks is calculated using the van der Waals equations, as follows:

$$pr^{\text{lp/hp}} = \frac{n^{\text{lp/hp}} \cdot R \cdot T^{\text{lp/hp}}}{V^{\text{lp/hp}} - n^{\text{lp/hp}} \cdot b} - a \cdot \frac{\left(n^{\text{lp/hp}}\right)^2}{\left(V^{\text{lp/hp}}\right)^2} \tag{15}$$

where $V^{\text{lp/hp}}$ is the volume, $n^{\text{lp/hp}}$ is the stored hydrogen in mol, and $T^{\text{lp/hp}}$ is the temperature of both storage tanks. Furthermore, a and b are constants that are calculated using the critical temperature T^{cr} and the critical pressure p^{cr}, as follows:

$$a = \frac{27 \cdot R^2 \cdot (T^{\text{cr}})^2}{64 \cdot p^{\text{cr}}}, \tag{16}$$

$$b = \frac{R \cdot T^{\text{cr}}}{8 \cdot p^{\text{cr}}}. \tag{17}$$

The battery model consists of a voltage model and a current model to calculate a change in the state of charge soc^{bat} and the battery voltage U^{bat}. The current model describes the difference between the main reaction current i^{bat} and the current at the battery terminal $i^{\text{bat,t}}$ [4], as follows:

$$i^{\text{bat}} = f(i^{\text{bat,t}}, U^{\text{bat}}). \tag{18}$$

The main reaction current is utilized to calculate a change in the state of charge of the battery, as follows:

$$soc_{i+1}^{\text{bat}} = soc_i^{\text{bat}} + \frac{i^{\text{bat}}}{Q^{\text{nom}}} \cdot \Delta t \tag{19}$$

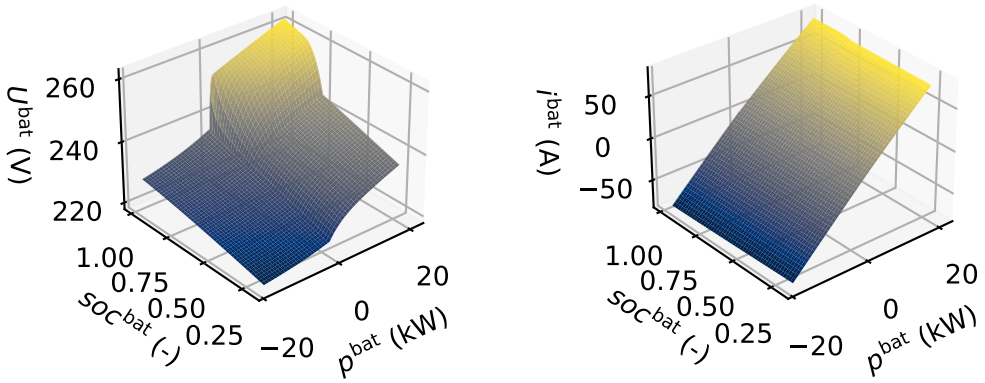
where Q^{nom} = 1380 Ah is the nominal battery capacity. The current at the battery terminal is utilized to calculate the battery power as follows:

$$p^{\text{bat}} = i^{\text{bat,t}} \cdot U^{\text{bat}}. \tag{20}$$

The battery voltage is equal to the voltage of the DC busbar and a function of the state of charge and the main reaction current i^{bat}, as follows:

$$U^{\text{bat}} = f(i^{\text{bat}}, soc^{\text{bat}}). \tag{21}$$

The state of charge is limited to values between 20% and 100%. A visualization of the voltage dependency of the battery on the state of charge and the charging and discharging power, as well as a visualization of the dependency of the main reaction current on the state of charge and the battery power, is shown in Figure 4. A detailed description of the battery model, as well as a validation of the model with experimental data, can be found in [4].



(**a**) Battery Voltage (**b**) Main Reaction Current

Figure 4. Nonlinear models of the battery voltage and the main reaction current.

The oxygen storage tank was not explicitly modeled within the simulation model of Ulleberg [4]. This work further simplifies Ulleberg's energy system by focusing on the energy storage system. Therefore, the PV system is not modeled, but the real-world measurements of the PV power are used directly as input for the simulation. One further adaptation is to increase the storage capacity of the high-pressure hydrogen storage tank by a factor of 1.3 so that the storage capacity is not exceeded.

The data for the electricity demand and the PV power are real-world measurements recorded during the operation of the energy storage system. The data from the year 1997 with maximal temporal resolution of 1-min timesteps were utilized in this work. Gaps in the time series are filled with the closest available data point. Around 3% of all data points for the simulation are generated this way. However, only 28 gaps exist that are longer than 1 h. A visualization of the corrected electricity demand and the corrected PV power is shown in Figure 5.

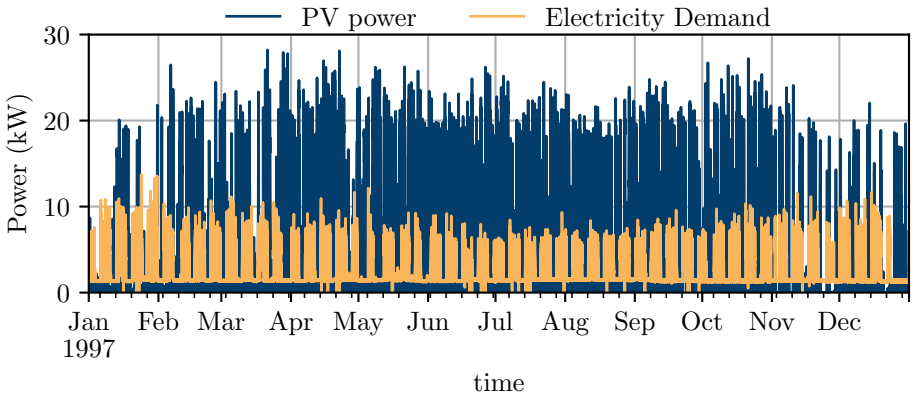


Figure 5. Corrected power demand and supply for the PHOEBUS Energy System during the year 1997.

2.2. Detailed Optimization Model

In the following section, we derive the novel MILP optimization models that are utilized in the scope of the MPC framework to derive optimal setpoints for the simulation model explained in Section 2.1. We derive the piecewise linear models by simulating the operational behavior of each component within its operational area and using the derived data as input for the toolbox LinMOG [42]. A detailed description of the workflow can be found in [41].

The component-oriented open-source framework COMANDO [53] is utilized to derive all optimization models in this and the following section. The detailed model of the energy system needs some simplifications to reduce its complexity. The first simplification is to preprocess the electrical energy consumed by the electricity demand. Therefore, the electricity consumption at the DC side of the inverter is calculated. Furthermore, the electrolyzer and the fuel cell models are lumped together with their respective DC/DC converters to reduce the number of piecewise linear models.

In the following, the MILP formulations for the piecewise linear models are not stated since the formulations are automatically derived using the modeling toolbox LinMOG [42] described in [41]. Each piecewise linear model allows only operating points on the visualized planes when the component is turned on. The 209 additional equations that are added for the detailed model and the 111 equations that are added for the simplified model are available in Appendix A.

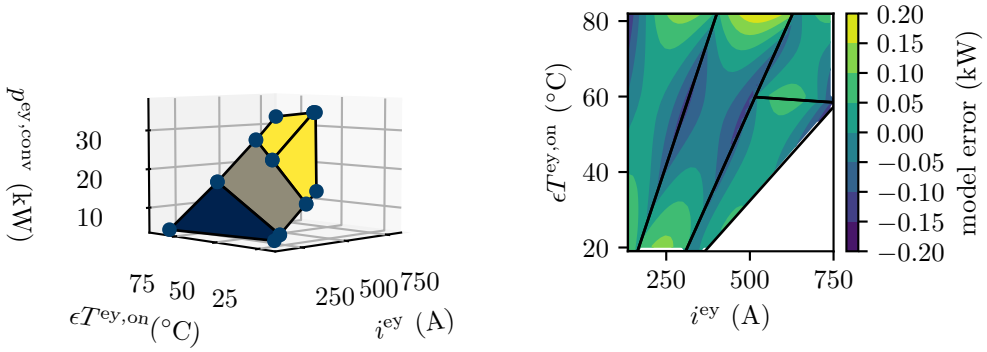
2.2.1. Electrolyzer

Multiple piecewise linear models are needed to describe the electrolyzer's operation accurately. First, the power input of the electrolyzer is modeled to enable a calculation of the energy balance around the DC busbar. Thus, a bivariate model for power input into the converter of the electrolyzer $p^{\text{ey,conv}}$ as a function of the temperature $\epsilon T^{\text{ey,on}}$ and the current i^{ey} is derived by sampling the operational area of the electrolyzer and simulating the electricity consumption. The piecewise linear model and the modeling error are shown in Figure 6. The piecewise linear model is utilized to predict the power output as a function of the electrolyzer temperature and current to predict the system response to a current setpoint i^{ey} that is utilized for model predictive control.

The temperature $\epsilon T^{\text{ey,on}}$ becomes zero when the electrolyzer is turned off, enabling the electrolyzer to shut down, described as follows:

$$\epsilon T_i^{\text{ey,on}} = T_i^{\text{ey}} \cdot \gamma_i^{\text{op,ey}} \tag{22}$$

where $\gamma_i^{\text{op,ey}}$ is a binary variable indicating the operational status. Equation (22) is linearized for the optimization problem using Equation (30).



(**a**) Piecewise linear model. (**b**) Modeling error.

Figure 6. Piecewise linear model of the relationship between the power consumption, the current, and the temperature of the electrolyzer. The piecewise linear model is depicted in (**a**), and the modeling error is visualized in (**b**).

The electrolyzer of the PHOEBUS Energy System exerts an almost constant Faraday efficiency over the whole operational area. Therefore, the nonlinear effects of the Faraday efficiency are neglected in the optimization problem. Thus, the hydrogen production is calculated by the following linear equation:

$$n_i^{\mathrm{H2,ey}} = c_1^{\mathrm{ey}} \cdot \gamma_i^{\mathrm{op,ey}} + c_2^{\mathrm{ey}} \cdot i_i^{\mathrm{ey}}, \tag{23}$$

where $n_i^{\mathrm{H2,ey}}$ is the hydrogen production, $c_1^{\mathrm{ey}} = -4.157 \cdot 10^{-4}$ and $c_2^{\mathrm{ey}} = 1.084 \cdot 10^{-4}$ are two constants.

The temperature change of the electrolyzer depends on its operational status, as explained in Section 2.1. Therefore, two variables $\Delta T_i^{\mathrm{ey,off}}$ and $\Delta T_i^{\mathrm{ey,on}}$ are needed to model the temperature change, as follows:

$$T_{i+1}^{\mathrm{ey}} = T_i^{\mathrm{ey}} + \left(\Delta T_i^{\mathrm{ey,off}} + \Delta T_i^{\mathrm{ey,on}}\right) \cdot \Delta t^{\mathrm{opt}}, \tag{24}$$

where $\Delta T_i^{\mathrm{ey,off}}$ is the temperature change when the electrolyzer is turned off, $\Delta T_i^{\mathrm{ey,on}}$ is the temperature change when the electrolyzer is turned on, and Δt^{opt} is the time step width of the optimization problem. The temperature change while the electrolyzer is turned off can be modeled as a linear function, as follows:

$$\Delta T_i^{\mathrm{ey,off}} = c_3^{\mathrm{ey}} \cdot \left(1 - \gamma_i^{\mathrm{op,ey}}\right) - c_4^{\mathrm{ey}} \cdot \epsilon T_i^{\mathrm{ey,off}}, \tag{25}$$

where $c_3^{\mathrm{ey}} = 0.0115$ and $c_4^{\mathrm{ey}} = 5.749 \cdot 10^{-4}$ are two constants, and $\epsilon T_i^{\mathrm{ey,off}}$ the temperature of the electrolyzer when it is turned off that is defined by the following:

$$\epsilon T_i^{\mathrm{ey,off}} = (1 - \gamma_i^{\mathrm{op,ey}}) \cdot T_i^{\mathrm{ey}}. \tag{26}$$

By using $\epsilon T_i^{\mathrm{ey,off}}$, the right-hand side of Equation (25) becomes zero if the electrolyzer is turned on. To linearize Equation (26), the following equations are utilized:

$$\epsilon T_i^{\mathrm{ey,off}} \leq \left(1 - \gamma_i^{\mathrm{op,ey}}\right) \cdot T^{\mathrm{ey,max}}, \tag{27}$$

$$\epsilon T_i^{\mathrm{ey,off}} + \gamma_i^{\mathrm{op,ey}} \cdot T^{\mathrm{ey,max}} \geq T_i^{\mathrm{ey}}, \tag{28}$$

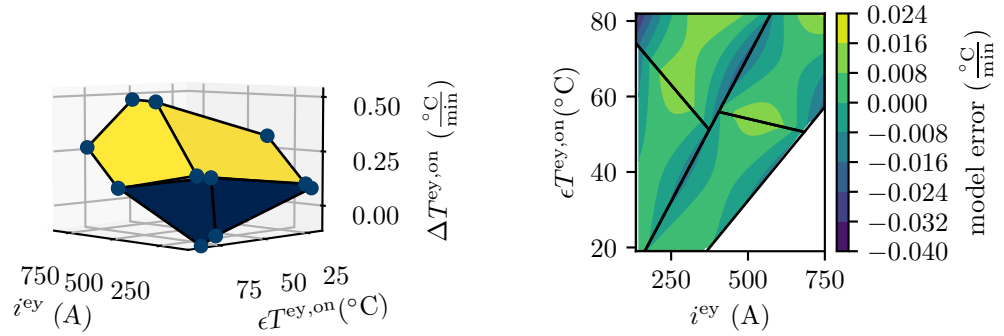
$$\epsilon T_i^{\mathrm{ey,off}} \leq T_i^{\mathrm{ey}}, \tag{29}$$

where $T^{\mathrm{ey,max}}$ is the maximal temperature of the electrolyzer. Next, a model for the temperature change of the electrolyzer when it is turned on $\Delta T_i^{\mathrm{ey,on}}$ is derived. Therefore, a piecewise linear model for the temperature changes of the electrolyzer when it is turned on $\Delta T^{\mathrm{ey,on}}$ at a given temperature $\epsilon T^{\mathrm{ey,on}}$ and input current i^{ey} is derived. For this, the operational area of the electrolyzer is sampled by setting a temperature and a current at the beginning of each timestep and simulating the temperature at the end of the timestep. This leads to a model as visualized in Figure 7a with a modeling error visualized in Figure 7b.

The piecewise linear model utilizes $\epsilon T_i^{\mathrm{ey,on}}$ as model input such that $\Delta T_i^{\mathrm{ey,on}} = 0$ when the electrolyzer is turned off. Since $\epsilon T_i^{\mathrm{ey,off}}$ is defined, $\epsilon T_i^{\mathrm{ey,on}}$ is derived by the following:

$$\epsilon T_i^{\mathrm{ey,on}} = T_i^{\mathrm{ey}} - \epsilon T_i^{\mathrm{ey,off}}. \tag{30}$$

Using the linear models and Equations (25)–(30) and the linear model visualized in Figure 7a, temperature changes of the electrolyzer can be accurately modeled.



(**a**) Piecewise linear model. (**b**) Modeling error.

Figure 7. Piecewise linear model and modeling error for the temperature changes of the electrolyzer with respect to its current and temperature.

The electrolyzer's operation is further adapted to reduce its degradation. In this work, the degradation caused by ramping and start-up and shutdown cycles is considered similar to Garcia-Torres et al. [19]. To reduce the number of start-up and shutdown cycles, a minimal operational $t^{\mathrm{ey,op}}$ and shutdown time $t^{\mathrm{ey,sd}}$ are considered similar to Fan et al. [21]. Furthermore, an additional term is added to the objective function to reduce the number of start-ups, shutdowns, and the ramping of the electrolyzer. The following equations enforce the minimal operational time and the minimal shutdown time:

$$st_i^{\mathrm{ey}} \geq \gamma_i^{\mathrm{op,ey}} - \gamma_{i-1}^{\mathrm{op,ey}}, \tag{31}$$

$$sd_i^{\mathrm{ey}} \geq \gamma_{i-1}^{\mathrm{op,ey}} - \gamma_i^{\mathrm{op,ey}}, \tag{32}$$

$$st_i^{\mathrm{ey}} \cdot N^{\mathrm{ey,op}} \leq \sum_{j=i}^{i+N^{\mathrm{ey,op}}} \gamma_j^{\mathrm{op,ey}}, \tag{33}$$

$$\left(1 - sd_i^{\mathrm{ey}}\right) \cdot N^{\mathrm{ey,sd}} \leq \sum_{j=i}^{i+N^{\mathrm{ey,sd}}} \gamma_j^{\mathrm{op,ey}}, \tag{34}$$

$$\sum_{j=0}^{N^{\mathrm{ey,st,init}}} st_j^{\mathrm{ey}} = 0, \tag{35}$$

$$\sum_{j=0}^{N^{\mathrm{ey,st,init}}} sd_j^{\mathrm{ey}} = 0. \tag{36}$$

In Equations (31)–(36) st_i^{ey} is a variable indicating a start-up of the electrolyzer at timestep i, sd_i^{ey} is a variable indicating a shutdown of the electrolyzer at timestep i, $N^{\mathrm{ey,op}}$ is the number of timesteps for the minimal operational time, and $N^{\mathrm{ey,sd}}$ is the number of timesteps for the minimal shutdown time. The initial operational status $\gamma^{\mathrm{op,ey,init}}$ and the number of timesteps in the initial state $N^{\mathrm{ey,st,init}}$ are parameters derived in a preprocessing step. Note that st_i^{ey} and sd_i^{ey} are not fixed to 0 if no start-up or shutdown occurs. Values of $t^{\mathrm{ey,op}} = t^{\mathrm{ey,sd}} = 2$ h were selected, similar to those used by Fan et al. [21], as this approach resulted in a reduced number of start-ups and shutdowns of the electrolyzer. The number of time steps $N^{\mathrm{ey,op}}$ and $N^{\mathrm{ey,sd}}$ in the operational and shutdown state can be calculated by the following:

$$N^{\mathrm{ey,sd}} = N^{\mathrm{ey,sd}} = \frac{t^{\mathrm{ey,op}}}{\Delta t^{\mathrm{opt}}} \tag{37}$$

since a constant timestep width Δt^{opt} is considered in this work.

The ramping r_i^{ey} in each timestep i can be modeled by the following:

$$r_i^{\text{ey}} \geq p_i^{\text{ey,conv}} - p_{i-1}^{\text{ey,conv}}, \tag{38}$$

$$r_i^{\text{ey}} \geq p_{i-1}^{\text{ey,conv}} - p_i^{\text{ey,conv}}. \tag{39}$$

The additional term for the objective function, designed to reduce the degradation of the electrolyzer J^{ey}, takes the following form:

$$J_i^{\text{ey}} = \frac{r_i^{\text{ey}}}{c_5^{\text{ey}}} + \left(st_i^{\text{ey}} + sd_i^{\text{ey}}\right) \cdot c_6^{\text{ey}} \tag{40}$$

where c_5^{ey}, and c_6^{ey} are constants to adjust the relative weight between a focus on ramping or start-up and shutdown cycles, depending on the desired strategy of the system operator. As stated by Garcia-Torres et al. [19], frequent start-ups and ramping of the electrolyzer drive degradation of the electrolyzer. However, as the system is not connected to the grid, a purely economic consideration of degradation effects as done by Garcia-Torres et al. [19] might not lead to the optimal strategy with regard to energy supply security. Thus, ramping and start-up effects for the electrolyzer are considered, but a different set of parameters from those used by Garcia-Torres et al. [19] is selected to reduce the number of start-ups and ramping while increasing the energy stored within both energy storage systems. In this work, the factors $c_5^{\text{ey}} = 10$ and $c_6^{\text{ey}} = 60$ led to a reduction of start-ups and shutdowns while not overly focusing on the degradation in comparison to storing energy within the hydrogen storage system. However, both values could be adapted by a system operator to adapt the operational strategy.

2.2.2. Fuel Cell

First, a piecewise linear model for the fuel cell operation is derived. The power output depends on the fuel cell current i^{fc} and the voltage at the DC busbar, as the fuel cell and its DC/DC converter are lumped together in the optimization model. The piecewise linear model derived for the fuel cell is shown in Figure 8a while the modeling error is shown in Figure 8b. The piecewise linear is generated using the modeling toolbox as described in [41]. The piecewise linear model is utilized to predict the power output of the fuel cell as a function of the bus voltage and the current i^{fc} that is utilized as a setpoint in the MPC framework.

The hydrogen consumption is modeled as a simple linear function as the Faraday efficiency is constant in the operating range of the fuel cell. Thus, the following function, i.e.,

$$n_i^{\text{H2,fc}} = c_1^{\text{fc}} \cdot i_i^{\text{fc}} \tag{41}$$

is used to estimate the hydrogen consumption $n_i^{\text{H2,fc}}$ as a function of the output current i_i^{fc} and a constant $c_1^{\text{fc}} = 0.00027781$ that was derived from the operational behavior of the simulation model.

Furthermore, a binary variable $\gamma_i^{\text{op,fc}}$ is introduced to indicate the operational state of the fuel cell. An additional variable needs to be introduced to allow a shutdown of the fuel cell, i.e.,

$$\epsilon U_i^{\text{bus}} = \gamma_i^{\text{op,fc}} \cdot U^{\text{bus}} \tag{42}$$

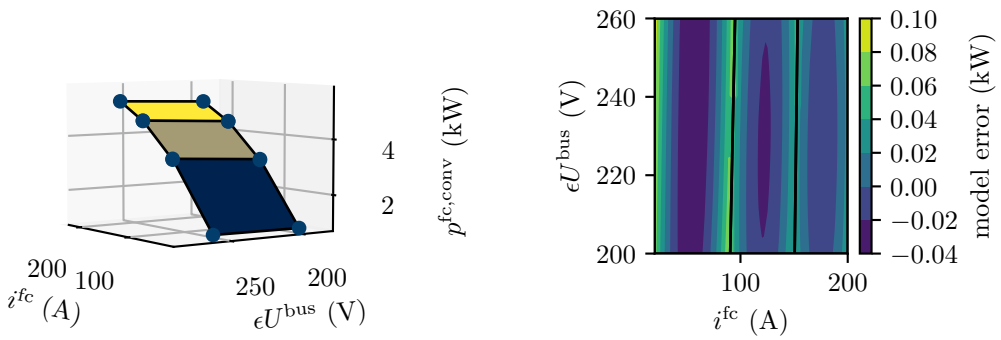
which is utilized as an input for the piecewise linear model to avoid constraint violations when the fuel cell is turned off. The linearization of Equation (42) takes the following form:

$$\epsilon U_i^{\text{bus}} \leq \gamma_i^{\text{op,fc}} \cdot U^{\text{bus,max}} \tag{43}$$

$$\epsilon U_i^{\text{bus}} + \left(1 - \gamma_i^{\text{op,fc}}\right) \cdot U^{\text{bus,max}} \geq U_i^{\text{bus}} \tag{44}$$

$$\epsilon U_i^{\text{bus}} \leq U_i^{\text{bus}} \tag{45}$$

where $U^{\text{bus,max}}$ is the maximal bus voltage.



(**a**) Piecewise linear model. (**b**) Modeling error.

Figure 8. Piecewise linear model and modeling error for the detailed model of the power output of the fuel cell.

Furthermore, this work considers the degradation caused by ramping, start-up, and shutdown cycles similar to assumptions in literature [19]. Therefore, to decrease the degradation of the fuel cell ramping, start-up and shutdown costs are added to the objective function. The ramping of the fuel cell is calculated by the following:

$$r_i^{\text{fc}} \geq p_i^{\text{fc,conv}} - p_{i-1}^{\text{fc,conv}}, \tag{46}$$

$$r_i^{\text{fc}} \geq p_{i-1}^{\text{fc,conv}} - p_i^{\text{fc,conv}}. \tag{47}$$

Additionally, a constraint is added to the fuel cell model to increase the utilization of the battery, as follows:

$$\gamma_i^{\text{op,fc}} \leq \left(1 + c_2^{\text{fc}}\right) - soc_i^{\text{bat}}, \tag{48}$$

where c_2^{fc} is a constant that describes the battery state of charge soc_i^{bat} at which the fuel cell can be turned on. In this work, a factor $c_2^{\text{fc}} = 0.4$ is utilized. Equation (48) is added to the optimization problem instead of a minimal operational and shutdown time to reduce the number of start-ups and shutdowns. However, an additional term in the objective function J_i^{fc} is utilized for the fuel cell that penalizes ramping r_i^{fc}, start-ups st^{fc}, and shutdowns sd^{fc} to reduce the degradation of the fuel cell further. The start-ups st^{fc} and shutdowns sd^{fc} are calculated by the following:

$$st_i^{\text{fc}} \geq \gamma_i^{\text{op,fc}} - \gamma_{i-1}^{\text{op,fc}}, \tag{49}$$

$$sd_i^{\text{fc}} \geq \gamma_{i-1}^{\text{op,fc}} - \gamma_i^{\text{op,fc}}, \tag{50}$$

using the binary variable $\gamma_i^{\text{op,fc}}$ that indicates the operational state of the fuel cell. The term added to the objective function for the fuel cell takes the following form:

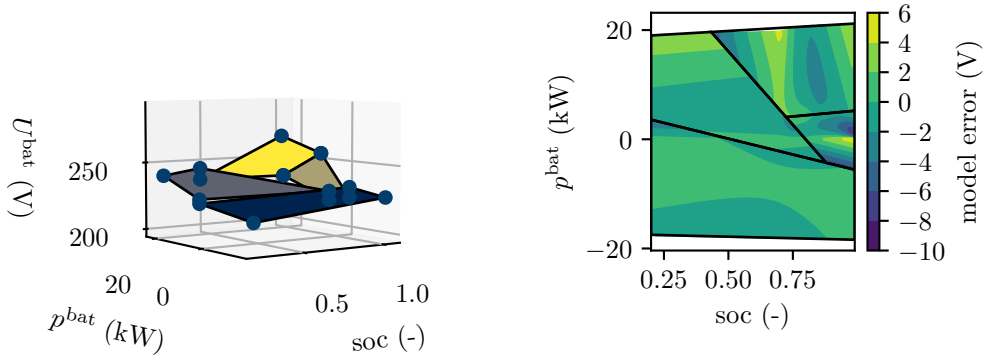
$$J_i^{\text{fc}} = r_i^{\text{fc}} \cdot c_3^{\text{fc}} + \left(st_i^{\text{fc}} + sd_i^{\text{fc}}\right) \cdot c_4^{\text{fc}} \tag{51}$$

where c_3^{fc} and c_4^{fc} are constants. In this work, values $c_3^{\text{fc}} = 0.5$ and $c_4^{\text{fc}} = 200$ were selected which led to a reduced ramping of the fuel cell and a reduced number of start-ups while still operating the fuel cell if necessary.

2.2.3. Battery

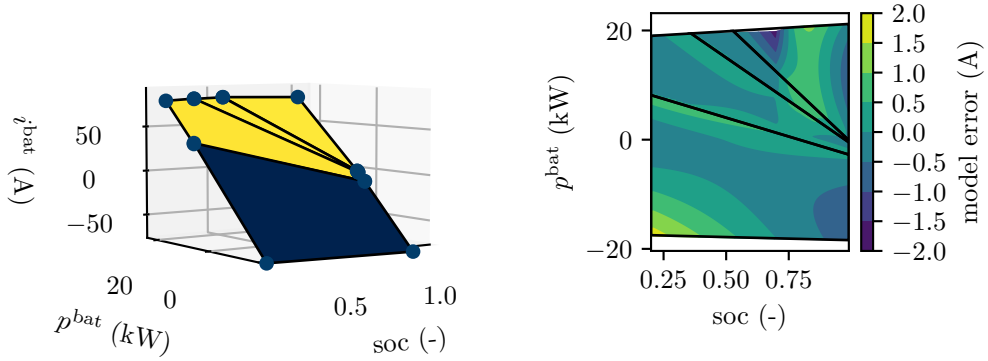
The operational behavior of the battery is modeled with two piecewise linear models. The first model estimates the battery voltage depending on the battery power and the state of charge. Figure 9a visualizes the piecewise linear model while the modeling error is visualized in Figure 9b. The second piecewise linear model estimates the main reaction

current of the battery as a function of the charging and discharging power and the state of charge of the battery. The piecewise linear model derived for the main reaction current of the battery is shown in Figure 10a, and the modeling error is visualized in Figure 10b. The piecewise linear models for the battery are utilized to estimate the battery voltage and the main reaction current to accurately predict the state of charge and the voltage of the DC busbar. The battery does not receive setpoints from the MPC or the HBC. However, an inadequate estimation of the battery state of charge is essential for the control of the energy system.



(**a**) Piecewise linear model. (**b**) Modeling error.

Figure 9. Piecewise linear model of the relationship between the power, the state of charge, and the voltage of the battery. The piecewise linear model is depicted in (**a**), and the modeling error is visualized in (**b**).



(**a**) Piecewise linear model. (**b**) Modeling error.

Figure 10. Piecewise linear model of the relationship between the power, the state of charge, and the current of the battery. The piecewise linear model is depicted in (**a**), and the modeling error is visualized in (**b**).

A change in the state of charge of the battery $\Delta soc_i^{\mathrm{bat}}$ is calculated using the main reaction current i_i^{bat} divided by the nominal capacity Q^{nom}, as follows:

$$\Delta soc_i^{\mathrm{bat}} = \frac{i_i^{\mathrm{bat}}}{Q^{\mathrm{nom}}} \tag{52}$$

where $Q^{\mathrm{nom}} = 1380$ Ah. Next, the state of charge of the battery in the next timestep is calculated by the following:

$$soc_{i+1}^{\mathrm{bat}} = soc_i^{\mathrm{bat}} + \Delta soc_i^{\mathrm{bat}} \cdot \Delta t^{\mathrm{opt}}. \tag{53}$$

The PHOEBUS Energy System was a stand-alone energy system that achieved an all-year-long supply of renewable energies to meet the electricity demand. Therefore, supply safety is important for the operation of the energy storage system. Thus, additional terms

for the objective function are introduced for the operation of the battery that incentivizes energy storage but keeps the battery in a safe operational area. The first additional term J_1^{bat} incentivizes the storage of energy in the battery, while the second term J_2^{bat} disincentivizes the optimization problem from fully charging or discharging the battery. The additional term J_i^{bat} for the battery that takes the following form:

$$J_i^{\text{bat}} = c_1^{\text{bat}} \cdot J_{1,i}^{\text{bat}} + c_2^{\text{bat}} \cdot J_{2,i}^{\text{bat}} \tag{54}$$

where c_1^{bat} and c_2^{bat} are two factors to weigh the two operational goals of the battery; $J_{1,i}^{\text{bat}}$ and $J_{2,i}^{\text{bat}}$ are determined by the following:

$$J_{1,i}^{\text{bat}} \leq soc_i^{\text{bat}} \tag{55}$$
$$J_{1,i}^{\text{bat}} \leq c_5^{\text{bat}} \tag{56}$$
$$J_{2,i}^{\text{bat}} \geq c_3^{\text{bat}} - soc_i^{\text{bat}} \tag{57}$$
$$J_{2,i}^{\text{bat}} \geq soc_i^{\text{bat}} - c_4^{\text{bat}} \tag{58}$$
$$J_{2,i}^{\text{bat}} \geq 0 \tag{59}$$

were c_3^{bat}, c_4^{bat}, and c_5^{bat} are constants. With Equations (55) and (56), the battery is incentivized to charge the battery up to a state of charge of c_5^{bat}. Furthermore, Equations (57) and (58) penalize discharging the battery below a state of charge of c_3^{bat} and charging the battery over a state of charge of c_4^{bat} for energy supply security. This is done as the optimization problem is only an approximation of the simulation model and, thus, deviations between the predicted and simulated state of charge occur during operation. By introducing $J_{2,i}^{\text{bat}}$, the battery is kept between a state of charge of c_3^{bat} and c_4^{bat} and, therefore, the battery is operated in a save operational area. The values selected in this work are $c_1^{\text{bat}} = -1$, $c_2^{\text{bat}} = 5$, $c_3^{\text{bat}} = 0.3$, $c_4^{\text{bat}} = 0.9$ and $c_5^{\text{bat}} = 0.8$ as these values led to a good trade-off between efficient utilization of the available energy and energy supply security.

2.2.4. Pressure Storage

Both pressure storage tanks are modeled with linear equations. A change in the state of charge Δsoc_i^{ps} is calculated by the following:

$$\Delta soc_i^{\text{ps}} = \frac{n_i^{\text{H2,ps,in}} - n_i^{\text{H2,ps,out}}}{c^{\text{ps}}} \tag{60}$$

where $n_i^{\text{H2,ps,in}}$ is the inflow of hydrogen, $n_i^{\text{H2,ps,out}}$ is the outgoing hydrogen flow, and c^{ps} is the capacity of the pressure storage tanks. Next, the state of charge of the pressure storage tanks in the next timestep is calculated by the following:

$$soc_{i+1}^{\text{ps}} = soc_i^{\text{ps}} + \Delta soc_i^{\text{ps}} \cdot \Delta t^{\text{opt}}. \tag{61}$$

The storage capacity c^{ps} is derived in a pre-processing step by the following:

$$c^{\text{ps}} = n^{\text{H2,max}} - n^{\text{H2,min}} \tag{62}$$

where $n^{\text{H2,min}}$ is the minimal and $n^{\text{H2,max}}$ is the maximal amount of hydrogen in the pressure storage tanks. The values for the maximal and minimal amounts of hydrogen in the storage tanks $n^{\text{H2,max,hp}}$ = 150,862.4 mol, $n^{\text{H2,max,lp}}$ = 7128 mol, $n^{\text{H2,min,hp}}$ = 11,349 mol, $n^{\text{H2,min,lp}}$ = 2048 mol are derived from the simulation models of the low-pressure (lp) and high-pressure (hp) hydrogen storage tanks. Next, the pressure within the storage tanks is calculated using the state of charge, as follows:

$$pr_i^{\text{ps}} = pr^{\text{ps,min}} + \left(pr^{\text{ps,max}} - pr^{\text{ps,min}}\right) \cdot soc_i^{\text{ps}}. \tag{63}$$

The state of charge is utilized as an additional term for the objective function J_i^{ps} for the hydrogen storage tanks to incentivize energy storage:

$$J_i^{\text{ps}} = -soc_i^{ps}. \tag{64}$$

2.2.5. Compressor

The electricity consumption of the compressor depends on the hydrogen flow rate n_i^{comp}, the inlet pressure $pr_i^{\text{comp,in}}$, and the outlet pressure $pr_i^{\text{comp,out}}$. Thus, a piecewise linear function with three inputs and one output is derived. The probability density function of the modeling error Δp^{comp} is as follows:

$$\Delta p^{\text{comp}} = p^{\text{comp,pred}} - p^{\text{comp,sim}}, \tag{65}$$

where $p^{\text{comp,pred}}$ and $p^{\text{comp,sim}}$ are the predicted and simulated electricity consumption, as shown in Figure 11.

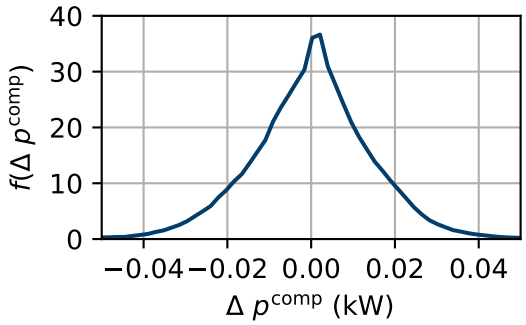


Figure 11. Probability density function of the modeling error for the model of the compressor.

To enable a shutdown of the compressor, two new variables for the input and output pressure, $\epsilon pr_i^{\text{comp,in}}$ and $\epsilon pr^{\text{comp,out}}$, need to be introduced, which are defined by the following:

$$\epsilon pr_i^{\text{comp,in}} = pr_i^{\text{comp,in}} \cdot \gamma_i^{\text{comp,op}} \tag{66}$$

$$\epsilon pr_i^{\text{comp,out}} = pr_i^{\text{comp,out}} \cdot \gamma_i^{\text{comp,op}} \tag{67}$$

where $\gamma_i^{\text{comp,op}}$ is a binary variable indicating the operational status of the compressor, $pr_i^{\text{comp,in}}$ and $pr_i^{\text{comp,out}}$ are the input and output pressure of the compressor, respectively. Both Equations (66) and (67) are linearized with the following:

$$\epsilon pr_i^{\text{comp,io}} \leq pr^{\text{comp,max,io}} \cdot \gamma_i^{\text{comp,op}} \tag{68}$$

$$\epsilon pr_i^{\text{comp,io}} + pr^{\text{comp,max,io}} \left(1 - \gamma_i^{\text{comp,op}}\right) \geq pr_i^{\text{comp,io}} \tag{69}$$

$$\epsilon pr_i^{\text{comp,io}} \leq pr_i^{\text{comp,io}} \tag{70}$$

where the superscript io represents input or output. $pr^{\text{comp,max,io}}$ is the maximal pressure at the inlet or the outlet. The maximal pressure within the pressure storage tanks determines the compressor's maximum inlet and outlet pressure. The electricity consumption of the compressor is neglected for the optimization problem as the electricity consumption of the compressor was not accounted for within the PHOEBUS project.

2.2.6. Energy System

The following equations are added to the optimization problem to model the connection between the following components:

$$p_i^{\text{fc,conv}} - p_i^{\text{ey,conv}} - p_i^{\text{bat}} - p_i^{\text{dem}} + p_i^{\text{pv}} = 0 \tag{71}$$

$$U_i^{\text{bat}} - U_i^{\text{bus}} = 0 \tag{72}$$

$$n_i^{\text{H2,ey}} - n_i^{\text{H2,ps,lp,in}} = 0 \tag{73}$$

$$n_i^{\text{H2,ps,lp,out}} - n_i^{\text{H2,comp,in}} = 0 \tag{74}$$

$$n_i^{\text{H2,ps,lp,out}} - n_i^{\text{H2,ps,hp,in}} = 0 \tag{75}$$

$$n_i^{\text{H2,ps,hp,out}} - n_i^{\text{H2,fc}} = 0 \tag{76}$$

$$pr_i^{\text{ps,lp}} - pr_i^{\text{comp,in}} = 0 \tag{77}$$

$$pr_i^{\text{ps,hp}} - pr_i^{\text{comp,out}} = 0 \tag{78}$$

A sketch of the connections between the components of the optimization problem is shown in Figure 12.

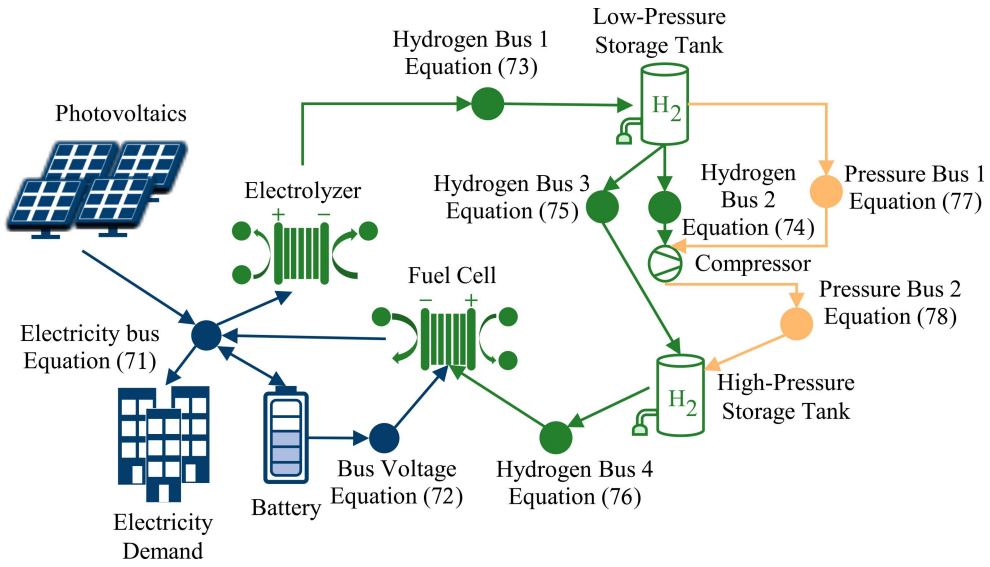


Figure 12. Sketch of the connections between components.

Next, the component objective terms are added up with their respective weightings w. Adding up the objectives in terms of each component is done to encompass all competing goals in one objective function. Thus, one novel operational objective J^{es} is derived for the energy system that both incentivizes energy storage with weights w^{bat}, $w^{\text{ps,lp}}$, and $w^{\text{ps,hp}}$, while considering degradation effects with weights w^{ey} and w^{fc}:

$$J^{\text{es}} = \sum_{i=0}^{N} \left(w^{\text{bat}} \cdot J_i^{\text{bat}} + w^{\text{ps,lp}} \cdot J_i^{\text{ps,lp}} + w^{\text{ps,hp}} \cdot J_i^{\text{ps,hp}} + w^{\text{ey}} \cdot J_i^{\text{ey}} + w^{\text{fc}} \cdot J_i^{\text{fc}} \right), \tag{79}$$

where N is the number of timesteps in the prediction horizon t^{pred}

$$N = \frac{t^{\text{pred}}}{\Delta t^{\text{opt}}}. \tag{80}$$

The weights for the term of the electrolyzer w^{ey} and the fuel cell w^{fc} are set to 1. The weights of the storage components are determined by an approach introduced in this work to calculate the total energy that each storage component can store. Thus, the energy distribution between the two storage solutions is done purely based on the component efficiencies. As shown in Section 4, this leads to a good long-term strategy where the combined state of charge of both storage technologies is maximized.

For the hydrogen components, the total energy that can be stored within the storage tank can be calculated by the capacity c^{ps} and the lower heating value $\Delta h^{\mathrm{H_2,lhv}} = 241.8$ kWh/mol. The weights of the storage components take the values $w_{\mathrm{bat}} = 303$, $w^{\mathrm{ps,lp}} = 341.21$, and $w^{\mathrm{ps,hp}} = 9370.65$.

2.3. Simplified Optimization Model

The main simplification for the simplified optimization model is the omission of any impacts by the bus voltage. Therefore, no model of the battery voltage is needed. Furthermore, the average charging and the average discharging efficiency are utilized to simplify the battery model further. Thus, the battery model does not contain any piecewise linear models in its simplified version. The calculated average charging efficiency is $c_6^{\mathrm{bat},} = 0.94$, and the discharging efficiency is $c_7^{\mathrm{bat}} = 0.97$. A change in the state of charge takes the following form:

$$\Delta soc_i^{\mathrm{bat}} = \frac{p_i^{\mathrm{bat,ch}} \cdot c_6^{\mathrm{bat},} - \frac{p_i^{\mathrm{bat,dc}}}{c_7^{\mathrm{bat}}}}{c^{\mathrm{bat,nom}}} \tag{81}$$

where $p_i^{\mathrm{bat,ch}}$ is the charging power and $p_i^{\mathrm{bat,dc}}$ is the discharging power and $c^{\mathrm{bat,nom}}$ is the battery capacity $c^{\mathrm{bat,nom}}$ = 303 kWh. The battery power p_i^{bat} is calculated by the following:

$$p_i^{\mathrm{bat}} = p_i^{\mathrm{bat,ch}} - p_i^{\mathrm{bat,dc}} \tag{82}$$

The fuel cell model is simplified to a univariate model as shown in Figure 13 since the bus voltage is omitted. However, since the simulation model remains unchanged, the model error is a function of the power output and the voltage of the DC busbar.

The hydrogen input is directly modeled as a function of the electricity output. Therefore, no additional equality constraint is needed to relate the hydrogen consumption with the stack current.

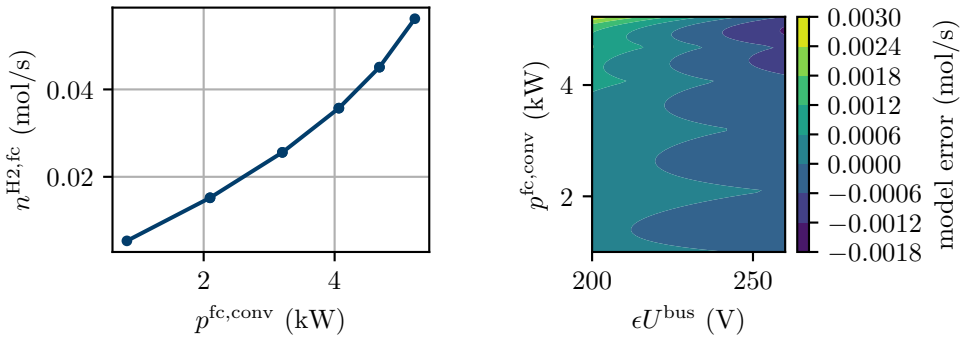
The electrical power consumed by the electrolyzer is modeled independently from the stack temperature to reduce the complexity of the model. The resulting piecewise linear model and the modeling error are shown in Figure 14a,b.

Furthermore, the hydrogen output is modeled directly as a function of the electricity input. To avoid overheating the electrolyzer, the stack temperature is modeled in the same way as described in Section 2.2.1. To utilize the same piecewise linear model, the electrolyzer current is calculated using the equality constraint, as follows:

$$n_i^{\mathrm{H2,ey}} = c_7^{\mathrm{ey}} \cdot \gamma_i^{ey,op} + c_8^{\mathrm{ey}} \cdot i_i^{\mathrm{ey}} \tag{83}$$

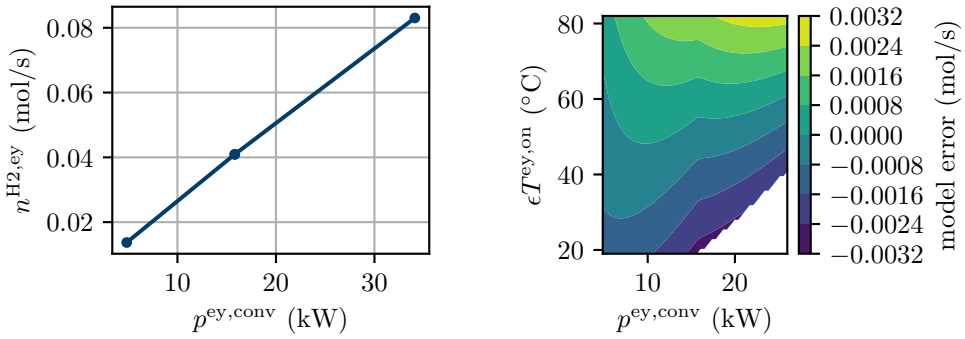
where the c_1^{ey} and c_2^{ey} are the same constants from Equation (23).

Using these simplifications, the number of continuous variables for a time horizon with 95-timesteps reduces from 9215 to 6745, and the number of integer variables reduces from 2565 to 1805. Furthermore, the number of constraints reduces from 24,219 to 15,574.



(**a**) Piecewise linear model. (**b**) Modeling error.

Figure 13. Simplified piecewise linear model and modeling error of the power output of the fuel cell.



(**a**) Piecewise linear model. (**b**) Modeling error.

Figure 14. Simplified piecewise linear model and modeling error for the model of the electrolyzer.

3. Case Study

An MPC framework and an HBC are developed in this work to study the performance of MPC in comparison to the HBC originally utilized for the project. Section 3.1 explains the settings of the MPC framework, while Section 3.2 describes the HBC.

3.1. Model Predictive Control Framework

The real-world data are available in a resolution of 1-min timesteps over the whole year of 1997, resulting in $N_{ts} = 525,969$ timesteps per year. Thus, the simulation of the energy system is run with a 1-min timestep width. The temporal resolution for the optimization problem is reduced to Δt^{opt} = 15 min or Δt^{opt} = 1 h timesteps by averaging the electricity demand and the PV power over the specified intervals. Thus, the number of time steps within the prediction horizon is reduced. Prediction horizons t^{pred} of 1 day up to 14 days are considered for the optimization problem as described in Section 2.2 or Section 2.3. A sketch of the MPC framework is shown in Figure 15. In this work, we utilize perfect foresight on the electricity demand and the PV power to evaluate the potential benefits of a detailed optimization model and the potential benefits of long prediction horizons.

The optimization problem is solved every 12 h to calculate new setpoints for the simulation system. Thus, the control horizon t^{cont} is 12 h long.

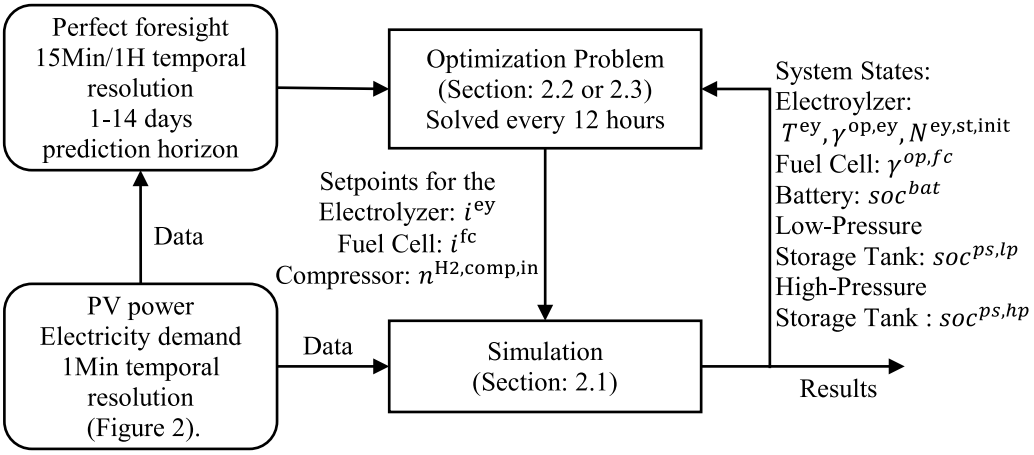


Figure 15. Sketch of the MPC framework.

The optimization problem is initialized in COMANDO [53] for the specified temporal resolution and prediction horizon. Next, the optimization problem is parameterized utilizing the resampled values for the PV power p_i^{pv} and the electricity demand p_i^{dem} within the prediction horizon. The system states in the current timestep t, $soc_t^{\text{ps,lp}}$, $soc_t^{\text{ps,hp}}$, soc_t^{bat} and T_t^{ey} are read from the simulation model. Furthermore, the operational state of the fuel cell $\gamma_t^{\text{op,fc}}$ and the electrolyzer $\gamma_t^{\text{op,ey}}$ and the time of the last shutdown and start-up of the electrolyzer are red from the simulation model. The system states are utilized to parameterize the optimization problem, as follows:

$$soc_t^{\text{ps,lp}} = soc_0^{\text{ps,lp}}, \tag{84}$$

$$soc_t^{\text{ps,hp}} = soc_0^{\text{ps,hp}}, \tag{85}$$

$$soc_t^{\text{bat}} = soc_0^{\text{bat}}, \tag{86}$$

$$T_t^{\text{ey}} = T_0^{\text{ey}}, \tag{87}$$

$$\gamma_t^{\text{op,ey}} = \gamma_0^{\text{op,ey}}, \tag{88}$$

$$\gamma_t^{\text{op,fc}} = \gamma_0^{\text{op,fc}}. \tag{89}$$

Moreover, using the time of the last start-up and shutdown of the electrolyzer, $N^{\text{ey,st,init}}$ is calculated and utilized in Equations (35) and (36) to parameterize the optimization problem. The optimization problem is solved to derive setpoints for the system control. The values derived from the optimization problem, namely the current setpoint for the electrolyzer i^{ey} and the fuel cell i^{fc} and the hydrogen flow through the compressor $n^{\text{H}_2,\text{comp,in}}$, are utilized as setpoints for the simulation model. Next, the system responses to the setpoints within the control horizon are simulated. A sketch of the interaction between the optimization results and the simulation model is shown in Figure 16.

The choices for the temporal resolution of the optimization problem Δt^{opt}, prediction horizon t^{pred}, and control horizon t^{cont} can influence the performance of the MPC. In the scope of this work, the impact of a temporal resolution Δt^{opt} and the prediction horizon t^{pred} are investigated. The optimization problem is solved using Gurobi [54] with a mixed integer programming (MIP) gap of 1% and a share of heuristics set to 10%.

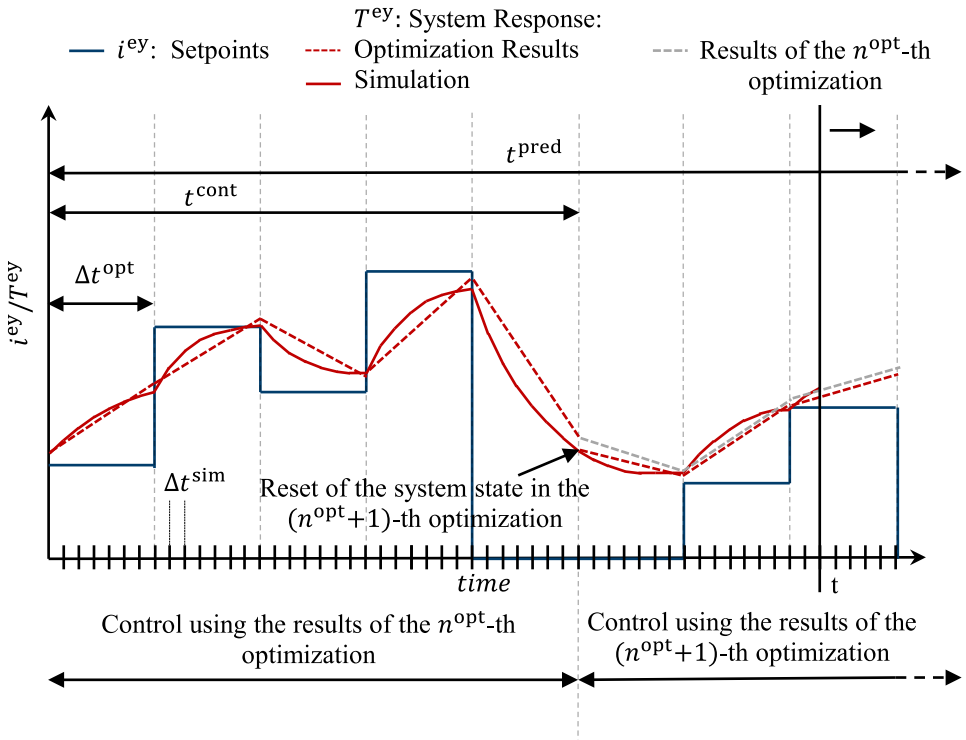


Figure 16. Sketch of the interaction between the optimization problem and the simulation model. Qualitative, exaggerated representation of the model error to visualize possible differences between the simulation and the optimization models.

3.2. Hysteresis Band Controller

The PHOEBUS Energy System was operated using a five-step control strategy, as explained in [52]. However, some adaptations are made to the original HBC based on the adaptations by Ulleberg [4]. The first adaptation is to neglect the safety limits of the hysteresis band controller. The components of the hydrogen system are capable of keeping the energy system within safe operating conditions without the need for safety limits on the state of charge of the battery. Therefore, only two hystereses, one for the lower bound of the battery state of charge and one for the upper bound of the state of charge are needed. The values for the HBC are set to a state of charge of the battery of 80% to turn the electrolyzer on and a value of 70% to switch the electrolyzer off again. One further improvement to the simple hysteresis band control is that the electrolyzer is turned off if the PV system generates no energy.

The fuel cell operation was fixed to one operating point in the real system. Therefore, the controller derived by Ulleberg [4] considered only a constant operating point for the fuel cell. One adaptation that Ulleberg made to the controller design is to adapt the hysteresis band according to the season. During the winter months, the fuel cell was turned on when the state of charge of the battery dropped below 45% and turned off again when the state of charge was higher than 50%. During the summer months, a value of 35% for the start-up and 40% for the shutdown was chosen. The constant operating point of the fuel cell significantly impacts the energy system's efficiency. Therefore, Ulleberg lowered the hydrogen flow to the fuel cell to 3 normal cubic meters per hour, which resulted in a power output of 4.3 kW. Since modern fuel cells can be operated with variable electricity output, this work adds an additional operating mode such that the fuel cell adjusts its energy production according to the energy deficit of the energy system. Furthermore, a limit for the maximum allowed electricity output of the fuel cell can be added so that operating points with very low efficiency are avoided. In the case study conducted in this work, a value of 5.3 kW was selected as the maximal power output of the fuel cell in the flexible

operating mode. A visualization of the hystereses for the electrolyzer and the fuel cell of the HBC is shown in Figure 17.

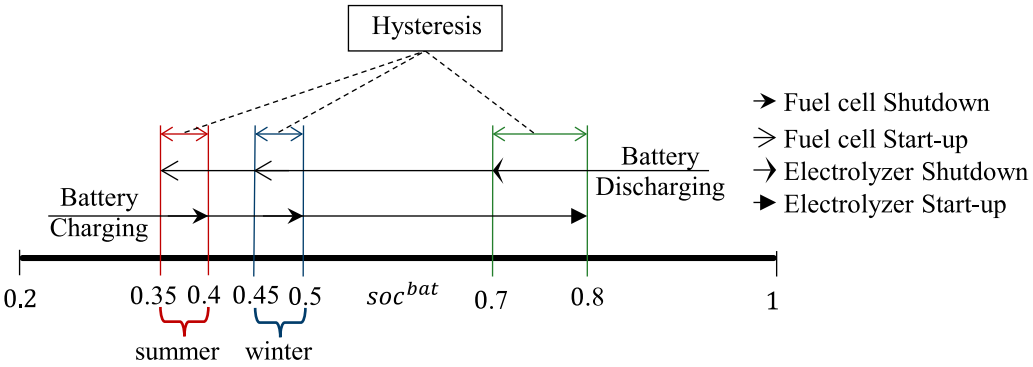


Figure 17. Sketch of the different hystereses utilized in the hysteresis band controller.

The compressor turned on when the pressure of the low-pressure hydrogen storage tank exceeded 5 bar and shut off again when the pressure dropped below 3 bar.

4. Results

First, the predictive capabilities of the optimization model are illustrated by comparing the optimization results with the simulation results in Section 4.1. Next, Section 4.2 investigates the system operation derived by an MPC with the detailed model and compares the results to an operation derived by an HBC. Furthermore, the resulting system operation derived by an MPC with the detailed model is compared with the system operation of multiple MPCs with the simplified model in Section 4.3. Finally, the impact of long prediction horizons and lower temporal resolutions is investigated. For each controller, the whole year of 1997 is simulated with the respective control strategy. Table 2 gives an overview of the different case studies.

Table 2. Overview of the controllers utilized in this work.

Hysteresis Band Controller			
Name	Description		
HBC B	HBC with fixed fuel cell hydrogen input of around 3 $\frac{nm^3}{h}$		
HBC F	HBC with a flexible fuel cell and maximal power output of 5.20 kW		
Model Predictive Controller			
Name	Optimization Model	Prediction Horizon	Temporal Resolution
MPC D 1D 15M	Detailed	1 Day	15 min
MPC S 1D 15M	Simplified	1 Day	15 min
MPC S 4D 15M	Simplified	4 Day	15 min
MPC S 4D 1H	Simplified	4 Day	1 h
MPC S 7D 1H	Simplified	7 Day	1 h
MPC S 7D 1H	Simplified	14 Day	1 h

4.1. Comparison between Optimization and Simulation Results

A comparison between the simulated system behavior and the system behavior prediction by the optimization problem is shown in this section to visualize the predictive capabilities of the detailed optimization model. In this section, the optimization problem is solved once with a prediction horizon of t^{pred} = 24 h. Next, the setpoints derived by solving the optimization problem are utilized as setpoints for the simulation model as described in Section 3.1. Thus, this section does not consider closed-loop model predictive control

but only showcases the predictive capabilities of the optimization model. In the following, the system behavior predicted by the optimization is called predicted system behavior for readability.

Figure 18 shows the PV power at the DC busbar and electricity demand at the DC side of the DC/AC inverter with a temporal resolution of $\Delta t^{\text{sim}} = 1$ min for the simulation of the energy system and a temporal resolution $\Delta t^{\text{opt}} = 15$ min time steps utilized as input data for the optimization problem.

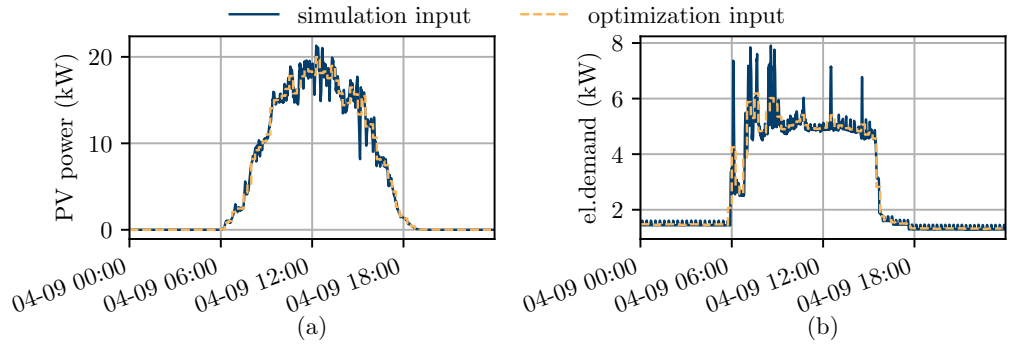


Figure 18. Visualization of the PV power and electricity demand on the 9 April with $\Delta t^{\text{sim}} = 1$ min and $\Delta t^{\text{opt}} = 15$ min. (**a**) shows a comparison between the PV power at the DC busbar and the data utilized for the parametrization of the PV power p^{pv} of the optimization problem. (**b**) shows the electricity demand at the DC busbar.

Figure 19 compares the predicted and simulated electricity consumption at the DC busbar and the predicted and simulated temperature of the electrolyzer. As shown, the detailed optimization model predicts the nonlinear dynamics of the electrolyzer and the DC/DC inverter with high accuracy. Some deviations can be observed in the temperature of the electrolyzer as predicted by the optimization problem. However, the deviations between the predicted and simulated temperatures are relatively small.

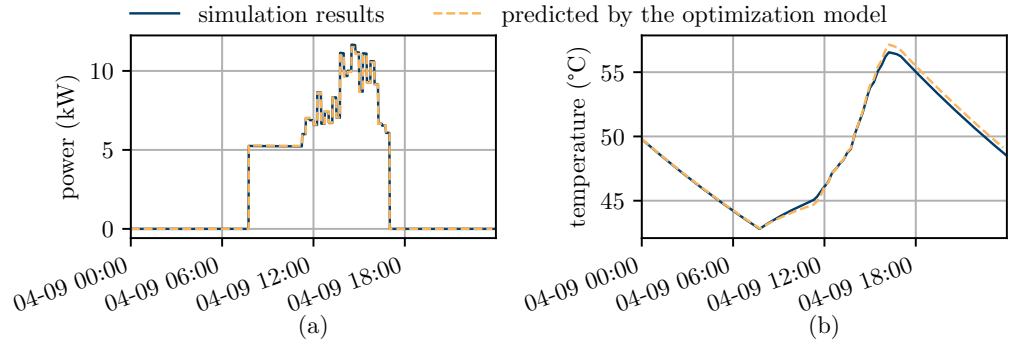


Figure 19. Visualization of the power input and the temperature of the electrolyzer with $\Delta t^{\text{sim}} = 1$ min and $\Delta t^{\text{opt}} = 15$ min. (**a**) compares the predicted and simulated electricity consumption of the electrolyzer at the DC busbar. (**b**) shows the predicted and simulated temperature of the electrolyzer.

The battery power and state of charge are shown in Figure 20. In Figure 20a, positive values indicate charging the battery, while negative values indicate discharging the battery. The short-term fluctuations of the PV power and electricity demand that are not accounted for in the data supplied to the optimization problem are compensated by the battery. These quick changes between loading and unloading lead to a deviation between the simulated and predicted state of charge.

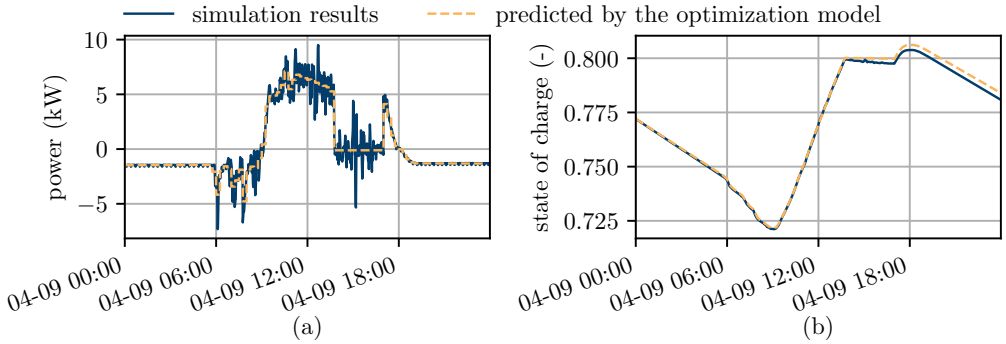


Figure 20. Visualization of the power input and the state of charge of the battery with $\Delta t^{\text{sim}} = 1$ min and $\Delta t^{\text{opt}} = 15$ min. (**a**) compares the predicted and simulated electricity input and output of the battery at the DC busbar; (**b**) shows the predicted and simulated state of charge of the battery.

Last, the hydrogen stored in the high-pressure and low-pressure storage tanks are visualized in Figure 21. As shown, the hydrogen content of both storage tanks is predicted accurately. As the fuel cell does not operate during the 9 April, no hydrogen is drawn from the pressure storage system.

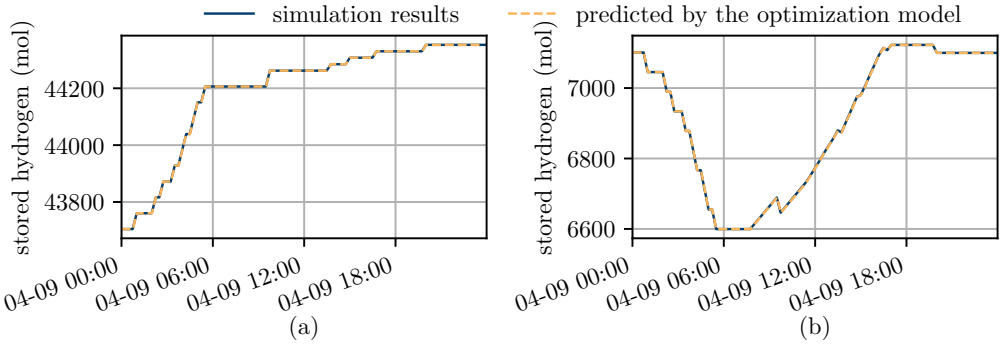


Figure 21. Visualization of the hydrogen stored in the high-pressure and low-pressure storage tanks with $\Delta t^{\text{sim}} = 1$ min and $\Delta t^{\text{opt}} = 15$ min. (**a**) compares the predicted and simulated stored hydrogen in the high-pressure storage tank. (**b**) shows the predicted and simulated stored hydrogen in the low-pressure storage tank.

In conclusion, this section illustrates that the optimization model can accurately predict the system dynamics. The battery mitigates the differences in energy availability caused by a lower temporal resolution of the optimization problem. This leads to slight deviations between the predicted and the simulated state of charge of the battery.

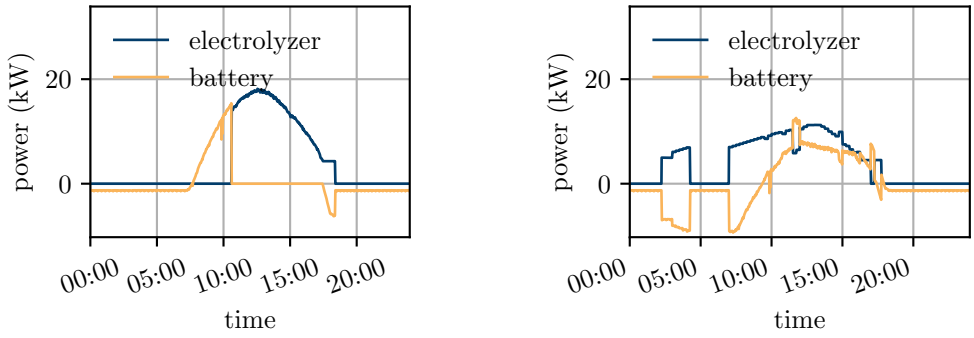
4.2. Comparison between the Model Predictive Controller and the Hysteresis Band Controller

First, the simulation results of two selected days are shown to visualize the difference between the operational strategy derived by the MPC and the HBC. All results shown in this section are the simulation results of the energy system controlled by different controllers. The results shown in Figures 22–26 are derived utilizing the HBC with a fixed volume flow to the fuel cell and the MPC with a detailed model and a prediction horizon of 1 day. The 9 March and 29 January are selected as exemplary days to show the difference between the operating strategy derived by the HBC and MPC on a day with excess energy from the PV park and on a day with an energy deficit. A quantitative comparison between the control strategies is made in Table 3.

Figure 23 visualizes the available PV power and the electricity demand on the 9 March.

The simulated system responses to the ambient conditions and the controller set points are shown in Figure 22. Figure 22a shows that the HBC first charges the battery until the state of charge reaches the defined threshold and then switches on the electrolyzer.

The electrolyzer is then operated so that the battery does not need to do any grid balancing. The electrolyzer operates until the sun sets. However, as the PV power drops below the electricity demand, electricity from the battery is needed to keep the electrolyzer running at its minimal part load operation. The MPC, in contrast, derives setpoints that divide the power between the battery and the electrolyzer, as shown in Figure 22b. Thus, the electrolyzer is operated at setpoints with a higher efficiency.



(**a**) HBC (**b**) MPC

Figure 22. Simulated system response to the control set points on the 9 March; (**a**) shows the system responses to the HBC and (**b**) shows the system responses to the MPC.

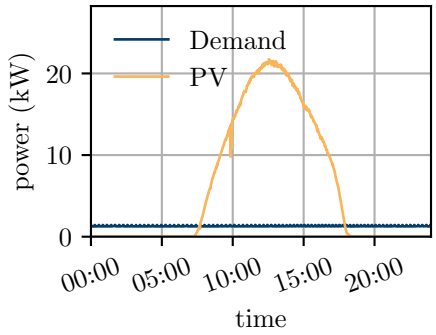


Figure 23. PV power and electricity demand on the 9 March 1997.

The PV power and the electricity demand for the 29 January are shown in Figure 24. As shown, no excess power is available during this day.

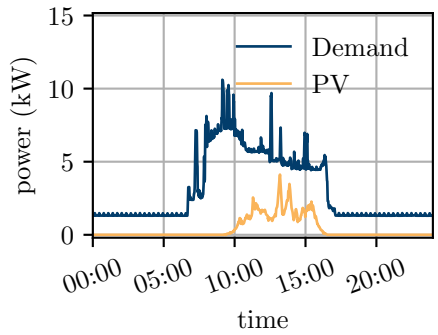
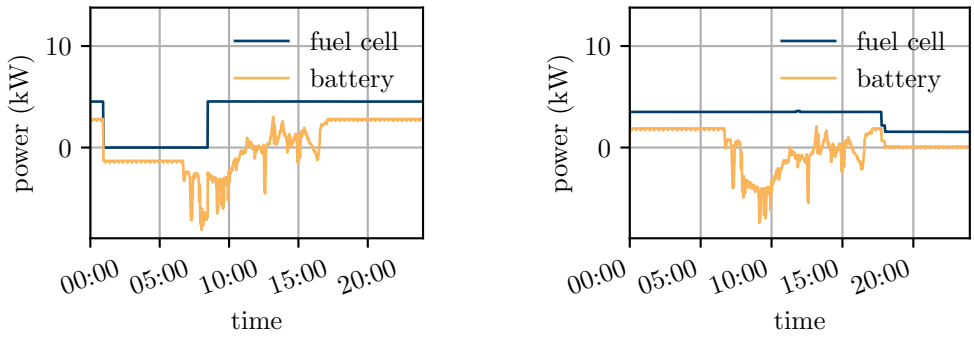


Figure 24. PV power and electricity demand on the 29 January 1997.

The simulated system responses to the ambient conditions and the control inputs are shown in Figure 25a and Figure 25b for the HBC and the MPC, respectively. As shown, the operation of both controllers is similar, but the MPC never switches off the fuel cell but maintains a steady operation throughout the night. Furthermore, the MPC operates the fuel cell at a lower part load to increase its efficiency.



(**a**) HBC (**b**) MPC

Figure 25. Simulated system response to the control set points on the 29 January. (**a**) shows the system responses to the HBC, and (**b**) shows the system responses to the MPC.

Furthermore, the total energy stored in the battery storage and the hydrogen storage e^{total} is calculated to compare the energy efficiency of both controllers:

$$e_i^{\text{total}} = soc_i^{\text{bat}} \cdot c^{\text{bat}} + \left(n_i^{\text{H2,hp}} + n_i^{\text{H2,lp}}\right) \cdot c^{\text{H2,mol}} \tag{90}$$

where $c^{\text{H2,mol}} = 0.06716$ kWh/mol is the lower heating value of hydrogen, and $n_i^{\text{H2,hp}}$ and $n_i^{\text{H2,lp}}$ are the hydrogen stored within the high-pressure and low-pressure storage tanks. The total energy stored in the energy storage system is visualized in Figure 26. As shown, the MPC utilizes the energy system more efficiently, such that more energy is stored at the end of the year compared to both HBCs. Furthermore, the MPC is the only controller that increases the total energy stored at the end of the year compared to the beginning.

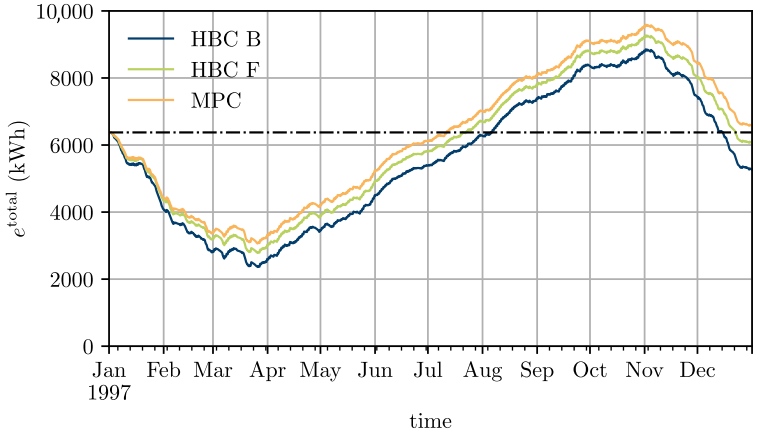


Figure 26. Comparison between the simulated total energy stored in the hybrid energy storage system controlled by the two different HBCs and the MPC with a detailed model.

The green plot in Figure 26 visualizes the simulated total energy stored in the hybrid energy storage system using the flexible HBC. As shown, even with the flexible operation of the fuel cell, the HBC utilizes the energy storage system more efficiently so that more energy is stored at the end of the year. Thus, the modified HBC performs significantly better than the HBC with a fixed hydrogen flow to the fuel cell since the fuel cell is utilized more efficiently.

Table 3 gives a detailed overview of the most important indicators for the system operation. All results shown in Table 3 are results of the simulation of the PHOEBUS Energy System controlled by the MPC and the two HBCs. The number of start-ups of the

electrolyzer $N^{\mathrm{st,ey}}$ and the number of start-ups of the fuel cell $N^{\mathrm{st,fc}}$ are derived by counting the transitions between the shutdown and the operational state of the electrolyzer and fuel cell, respectively. The average efficiencies of the fuel cell and electrolyzer are calculated by the following:

$$\eta^{\mathrm{ey}} = \frac{\sum_{i=1}^{N_{ts}} \left(n_i^{\mathrm{H2,ey}} \cdot c^{\mathrm{H2,mol}} \cdot \Delta t^{\mathrm{sim}} \right)}{\sum_{i=1}^{N_{ts}} p_i^{\mathrm{ey}} \cdot \Delta t^{\mathrm{sim}}} \tag{91}$$

$$\eta^{\mathrm{fc}} = \frac{\sum_{i=1}^{N_{ts}} p_i^{\mathrm{fc}} \cdot \Delta t^{\mathrm{sim}}}{\sum_{i=1}^{N_{ts}} \left(n_i^{\mathrm{H2,fc}} \cdot c^{\mathrm{H2,mol}} \cdot \Delta t^{\mathrm{sim}} \right)} \tag{92}$$

where η^{ey} is the average electrolyzer efficiency, and η^{fc} is the average fuel cell efficiency. Furthermore, the values for the ramping of the electrolyzer r^{ey} and the fuel cell r^{fc} are calculated by the following:

$$r^{\mathrm{fc}} = \sum_{i=1}^{N_{ts}} |p_i^{\mathrm{fc}} - p_{i-1}^{\mathrm{fc}}| \tag{93}$$

$$r^{\mathrm{ey}} = \sum_{i=1}^{N_{ts}} |p_i^{\mathrm{ey}} - p_{i-1}^{\mathrm{ey}}| \tag{94}$$

Finally, the electrical energy that is converted to hydrogen by the electrolyzer $e^{\mathrm{el,ey}}$ and the electrical energy that is produced by the fuel cell $e^{\mathrm{el,fc}}$ are calculated by the following:

$$e^{\mathrm{el,ey}} = \sum_{i=1}^{N_{ts}} p_i^{\mathrm{ey}} \cdot \Delta t^{\mathrm{sim}}, \tag{95}$$

$$e^{\mathrm{el,fc}} = \sum_{i=1}^{N_{ts}} p_i^{\mathrm{fc}} \cdot \Delta t^{\mathrm{sim}}. \tag{96}$$

Table 3. Comparison between the resulting key performance indicators for an MPC with a detailed model and two HBCs. All results are based on the results of the simulation of the energy system controlled by the MPC or the two HBCs.

	MPC D 1D 15M	**HBC B**	**HBC F**
Controller	MPC	HBC	HBC
Fuel Cell Operation	Flexible	Fixed Volume Flow	Flexible
Prediction Horizon	1 Day	-	-
Temporal Resolution	15 min	-	-
$e_{N_{ts}}^{\mathrm{total}}$ (kWh)	6570.65	5264.86	6061.73
η^{ey}	0.724	0.721	0.721
$e^{el,ey}$ (kWh)	9081.08	9276.62	9290.35
η^{fc}	0.591	0.512	0.563
$e^{el,fc}$ (kWh)	3708.91	3960.40	3905.51
$N^{\mathrm{st,ey}}$	326	161	160
r^{ey} (kW)	8439.16	33,948.79	34,042.73
$N^{\mathrm{st,fc}}$	24	93	27
r^{fc} (kW)	537.61	854.57	4780.54

Table 3 shows that the fuel cell and the electrolyzer are operated more efficiently using the MPC compared to both HBC approaches. The fuel cell efficiency increases are

especially noteworthy since the MPC operates the fuel cell more often at a lower part load. In this case study, the MPC uses the hydrogen storage system less than the HBC. Both the total electrical energy converted by the electrolyzer $e^{\mathrm{el,ey}}$ as well as the electrical energy produced by the fuel cell $e^{\mathrm{el,fc}}$ take smaller values for the energy system controlled by the MPC in comparison to the HBC. Thus, the whole energy system is used more efficiently as the battery efficiency is higher than the efficiency of the hydrogen storage system. This leads to an increase of the total energy stored at the end of the year by 8.3% compared to the HBC with a flexible fuel cell operation. Moreover, the ramping of the fuel cell and the electrolyzer decreased by more than 37% and 75%, respectively. However, one downside of the utilization of the MPC is the increased number of electrolyzer start-ups compared to both HBC controllers.

4.3. Comparison between MPC Runs

In the following, the simulation results of the PHOEBUS system controlled by different MPCs are compared with each other. All results shown in this section are the simulation results of the energy system controlled by different MPCs. First, the results derived from the MPC with the detailed system model are compared to the results derived from an MPC with the simplified model. Furthermore, the prediction horizon is increased to up to 14 days while reducing the temporal resolution to 1 h time steps. All results shown in Table 4 are simulation results of the PHOEBUS Energy System controlled by different MPCs.

Table 4. Comparison between the resulting key performance indicators for different MPCs. All results are based on the results of the simulation of the energy system controlled by different MPCs.

	MPC D 1D 15M	**MPC S 1D 15M**	**MPC S 4D 15M**	**MPC S 4D 1H**	**MPC S 7D 1H**	**MPC S 14D 1H**
Optimization Model	Detailed	Simplified	Simplified	Simplified	Simplified	Simplified
Prediction Horizon	1 Day	1 Day	4 Days	4 Days	7 Days	14 Days
Temporal Resolution	15 min	15 min	15 min	1 h	1 h	1 h
$e^{\mathrm{total}}_{N_{ts}}$ (kWh)	6570.65	6096.62	7037.81	6907.51	7070.36	7205.98
η^{ey}	0.724	0.728	0.727	0.725	0.727	0.731
$e^{el,ey}$ (kWh)	9081.08	9278.95	9052.45	8965.67	8973.24	8924.64
η^{fc}	0.591	0.593	0.616	0.617	0.624	0.63
$e^{el,fc}$ (kWh)	3708.91	4103.06	3585.76	3616.26	3571.90	3520.4
$N^{\mathrm{st,ey}}$	326	236	155	176	153	153
r^{ey} (kW)	8439.16	3601.19	3675.68	3665.34	2955.72	1963.08
$N^{\mathrm{st,fc}}$	24	31	26	23	23	24
r^{fc} (kW)	537.61	608.48	361.72	281.37	267.50	237.1
avg. run time (s)	44.81	26.53	70.02	27.05	38.30	66.54
max. run time (s)	548.67	50.08	189.32	82.82	79.86	192.75

The run time includes the initialization of the optimization problem in COMANDO, the parametrization of the optimization problem, the parsing of the problem to a Gurobi problem, the time for solving the optimization problem, and the simulation of the system responses for the control horizon of 12 h.

The maximum run time is below 10 min, while the control horizon is 12 h long. Thus, all investigated MPC controllers are real-time capable for this specific energy system. The detailed optimization problem leads to the highest run time even though a prediction horizon of 1 day with 15-min time steps is considered. Thus, it can be concluded that the additional piecewise linear models can drastically increase the optimization run time. The optimization problem with a 4-day prediction horizon and 15-min time steps contains the most time steps and leads to the highest average optimization run time. Furthermore,

the optimization problem with a one-day prediction horizon in a 15-min resolution and the optimization problem with four days in hourly resolution both contain 96 time steps and result in a similar average run time.

The MPC utilizing a simplified model of the PHOEBUS Energy System with a one-day prediction horizon performs worse than the MPC utilizing the detailed model. The total energy at the end of the year decreases by 7.7%, as the hydrogen storage system is utilized more often. The decrease in the total energy stored at the end of the year shows that the energy storage system is utilized less effectively. Thus, it can be concluded that utilizing the more accurate representation of the energy storage system in the optimization problem results in an improved performance of the MPC for this specific energy storage system. However, if the prediction horizon is increased to 4 days, the MPC performance increases compared to both MPCs with a one-day prediction horizon. This shows that for this energy system, a long prediction horizon can lead to an increased performance of the MPC. The total electricity stored at the end of the year increases by 15% compared to a prediction horizon of 1 day while decreasing the number of start-ups and the ramping of the fuel cell. A reduction of the temporal resolution to 1-h timesteps slightly decreases the performance of the MPC, showing that a higher temporal resolution results in a better performance. This might be due to an increased accuracy of the predicted PV power and electricity demand and a finer resolution of the control output of the MPC. However, if the prediction horizon is increased to 7 or 14 days, the negative effects of a lower temporal resolution are outweighed by the benefits of better long-term planning. By increasing the prediction horizon to 7 or 14 days, the total energy stored at the end of the year increases, while the number of start-ups and the ramping of the electrolyzer and the fuel cell decrease. Thus, it can be concluded that for the energy system investigated in this work, a long prediction horizon is more impactful than a good temporal resolution or a detailed model of the energy system. The efficiency of the fuel cell and the electrolyzer increase if long prediction horizons are used. Thus, the electrolyzer and fuel cell are operated more often at a lower part load when a long prediction horizon is considered due to the higher efficiency at lower part loads as shown in Figures 2 and 3. Furthermore, both the fuel cell and the electrolyzer are utilized less often if long prediction horizons are considered. Therefore, it can be concluded that the hydrogen storage system is utilized less often to meet the electricity demand.

5. Conclusions

This work shows the derivation of novel MILP optimization models for modeling hybrid battery-hydrogen energy storage systems that enable a direct description of the multidimensional component operational behavior. The models lead to an accurate representation of the complex operational behavior of the components such that system responses were predicted with high accuracy. The derived optimization model was utilized in a model predictive control framework to derive the optimal operational strategy for the PHOEBUS Energy System. The novel MILP optimization models allowed the MPC to make use of the energy storage system's nonlinear multidimensional dynamics, such as the variable temperature of the electrolyzer, to increase the efficiency of the energy storage system. Furthermore, a novel single objective function for the optimization problem was derived that incentivizes energy storage while considering degradation effects. The objective function was shown to be sufficient to derive a seasonal strategy for the energy storage system investigated in this work, even with a prediction horizon of just one day.

The potential benefits of MPC compared to heuristic controllers were demonstrated by simulating the system operation with both controllers for one year. Furthermore, a simplified optimization model was derived to investigate its impact on the effectiveness of model predictive control. The simplified optimization problem was shown to reduce the MPC's effectiveness but also the optimization run time. Thus, a longer prediction horizon could be investigated with the simplified optimization model.

This work shows that a long prediction horizon can be important for the long-term planning of this energy system. A more detailed model of the energy system and a

higher temporal resolution improved the performance of the MPC, but a long prediction horizon was found to increase the performance of the MPC the most for this energy system. However, the results derived in this work are based on perfect foresight regarding the generated PV power and electricity demand. Thus, future works might investigate the impact of forecast uncertainties on the performance of MPC with long prediction horizons.

In conclusion, MPC yielded improvements in all key performance indicators selected in this work. The best-performing MPC utilized a simplified model with a 14-day prediction horizon in a 1-h resolution. Comparing the best-performing HBC and the best MPC, the total energy stored at the end of the year increased by 18.9%, while the number of start-ups of the fuel cell and electrolyzer decreased by 11.1% and 4.4%, respectively. The ramping of the fuel cell was decreased by 72.2%, while the ramping of the electrolyzer was decreased by 94.3%. These drastic improvements are possible due to the utilization of perfect foresight on the generated PV power and electricity demand over 14 days. With a prediction horizon of only one day, the energy stored at the end of the year can be increased by 8.3%. In conclusion, this work shows a novel objective function for achieving seasonal energy storage with a model predictive controller for a stand-alone energy storage system by incentivizing energy storage. Furthermore, this work shows that considering long prediction horizons can be a key factor in the optimal utilization of the available energy.

Author Contributions: Conceptualization, A.H.; methodology, A.H.; software, A.H.; investigation, A.H.; writing—original draft preparation, A.H.; writing—review and editing, A.H., A.X., and D.M.; visualization, A.H.; supervision, A.X. and D.M.; project administration, A.X. and D.M.; funding acquisition, D.M. All authors have read and agreed to the published version of the manuscript.

Funding: The development of the framework was supported by the German Federal Ministry of Education and Research, grant number 03SF0573.

Data Availability Statement: The data presented in this study are currently not publicly available. The data will be made available by the authors on request.

Acknowledgments: The authors gratefully acknowledge the cooperation of IET-4 in providing operational data and descriptions of the PHOEBUS Energy System.

Conflicts of Interest: The authors declare that they have no known competing financial interests or personal relationships that could have appeared to influence the work reported in this paper.

Appendix A. Piecewise Linear Models

In the following, the piecewise linear models are stated in a generalized form, including the specific numeric values of all parameters. γ are binary variables of each linear element, x denotes the continuous variables, and a denotes the constants. Numbers in the superscripts refer to linear elements, while numbers in subscripts of continuous variables refer to input dimensions.

Appendix A.1. Electrolyzer Power

$$\gamma^{\mathrm{op,ey}} \cdot a_0^{\mathrm{ey,p}} + a_1^{\mathrm{ey,p}} \cdot i^{\mathrm{ey}} \leq 0 \tag{A1}$$

$$\gamma^{\mathrm{op,ey}} \cdot a_2^{\mathrm{ey,p}} - a_1^{\mathrm{ey,p}} \cdot i^{\mathrm{ey}} \leq 0 \tag{A2}$$

$$\gamma^{\mathrm{op,ey}} \cdot a_3^{\mathrm{ey,p}} - a_1^{\mathrm{ey,p}} \cdot \epsilon T^{\mathrm{ey,on}} \leq 0 \tag{A3}$$

$$\gamma^{\mathrm{op,ey}} \cdot a_4^{\mathrm{ey,p}} + a_1^{\mathrm{ey,p}} \cdot \epsilon T^{\mathrm{ey,on}} \leq 0 \tag{A4}$$

$$\gamma^{\mathrm{op,ey}} \cdot a_6^{\mathrm{ey,p}} + a_5^{\mathrm{ey,p}} \cdot i^{\mathrm{ey}} + a_7^{\mathrm{ey,p}} \cdot \epsilon T^{\mathrm{ey,on}} \leq 0 \tag{A5}$$

$$x_0^{0,\mathrm{ey,p}} \leq a_8^{\mathrm{ey,p}} \cdot \gamma^{0,\mathrm{ey,p}} \tag{A6}$$

$$x_0^{0,\mathrm{ey,p}} \geq 0 \tag{A7}$$

$$x_1^{0,ey,p} \leq -a_3^{ey,p} \cdot \gamma^{0,ey,p} \tag{A8}$$

$$x_1^{0,ey,p} \geq 0 \tag{A9}$$

$$x_0^{1,ey,p} \leq a_{10}^{ey,p} \cdot \gamma^{1,ey,p} \tag{A10}$$

$$x_0^{1,ey,p} \geq 0 \tag{A11}$$

$$x_1^{1,ey,p} \leq -a_3^{ey,p} \cdot \gamma^{1,ey,p} \tag{A12}$$

$$x_1^{1,ey,p} \geq 0 \tag{A13}$$

$$x_0^{2,ey,p} \leq a_{10}^{ey,p} \cdot \gamma^{2,ey,p} \tag{A14}$$

$$x_0^{2,ey,p} \geq 0 \tag{A15}$$

$$x_1^{2,ey,p} \leq a_{11}^{ey,p} \cdot \gamma^{2,ey,p} \tag{A16}$$

$$x_1^{2,ey,p} \geq 0 \tag{A17}$$

$$x_0^{3,ey,p} \leq a_{12}^{ey,p} \cdot \gamma^{3,ey,p} \tag{A18}$$

$$x_0^{3,ey,p} \geq 0 \tag{A19}$$

$$x_1^{3,ey,p} \leq -a_3^{ey,p} \cdot \gamma^{3,ey,p} \tag{A20}$$

$$x_1^{3,ey,p} \geq 0 \tag{A21}$$

$$a_{13}^{ey,p} \cdot x_0^{0,ey,p} + a_{14}^{ey,p} \cdot \gamma^{0,ey,p} + a_{15}^{ey,p} \cdot x_1^{0,ey,p} \leq 0 \tag{A22}$$

$$a_{16}^{ey,p} \cdot \gamma^{1,ey,p} + a_{17}^{ey,p} \cdot x_0^{1,ey,p} + a_{18}^{ey,p} \cdot x_1^{1,ey,p} \leq 0 \tag{A23}$$

$$a_{19}^{ey,p} \cdot \gamma^{1,ey,p} + a_{20}^{ey,p} \cdot x_1^{1,ey,p} + a_{21}^{ey,p} \cdot x_0^{1,ey,p} \leq 0 \tag{A24}$$

$$-a_{17}^{ey,p} \cdot x_0^{2,ey,p} - a_{18}^{ey,p} \cdot x_1^{2,ey,p} + a_{24}^{ey,p} \cdot \gamma^{2,ey,p} \leq 0 \tag{A25}$$

$$a_{19}^{ey,p} \cdot \gamma^{2,ey,p} + a_{20}^{ey,p} \cdot x_1^{2,ey,p} + a_{21}^{ey,p} \cdot x_0^{2,ey,p} \leq 0 \tag{A26}$$

$$-a_{21}^{ey,p} \cdot x_0^{3,ey,p} + a_{26}^{ey,p} \cdot \gamma^{3,ey,p} + a_{27}^{ey,p} \cdot x_1^{3,ey,p} \leq 0 \tag{A27}$$

$$-a_{14}^{ey,p} \cdot \gamma^{3,ey,p} - a_{15}^{ey,p} \cdot x_1^{3,ey,p} + a_{30}^{ey,p} \cdot x_0^{3,ey,p} \leq 0 \tag{A28}$$

$$\gamma^{0,ey,p} + \gamma^{1,ey,p} + \gamma^{2,ey,p} + \gamma^{3,ey,p} = \gamma^{op,ey} \tag{A29}$$

$$\begin{aligned} p^{ey} = {} & a_{31}^{ey,p} \cdot \gamma^{0,ey,p} + a_{32}^{ey,p} \cdot x_0^{0,ey,p} + a_{33}^{ey,p} \cdot x_0^{3,ey,p} \\ & + a_{34}^{ey,p} \cdot x_0^{2,ey,p} + a_{35}^{ey,p} \cdot x_0^{1,ey,p} + a_{36}^{ey,p} \cdot \gamma^{1,ey,p} \\ & + a_{37}^{ey,p} \cdot \gamma^{3,ey,p} + a_{38}^{ey,p} \cdot \gamma^{2,ey,p} + a_{39}^{ey,p} \cdot x_1^{3,ey,p} \\ & + a_{40}^{ey,p} \cdot x_1^{0,ey,p} + a_{41}^{ey,p} \cdot x_1^{2,ey,p} + a_{42}^{ey,p} \cdot x_1^{1,ey,p} \end{aligned} \tag{A30}$$

$$i^{ey} = x_0^{0,ey,p} + x_0^{1,ey,p} + x_0^{2,ey,p} + x_0^{3,ey,p} \tag{A31}$$

$$\epsilon T^{ey,on} = x_1^{0,ey,p} + x_1^{1,ey,p} + x_1^{2,ey,p} + x_1^{3,ey,p} \tag{A32}$$

Table A1. Constants for the piecewise linear model of the power output of the electrolyzer.

Constant	Value	Constant	Value	Constant	Value
$a_0^{\mathrm{ey,p}}$	135.0	$a_1^{\mathrm{ey,p}}$	−1.00	$a_2^{\mathrm{ey,p}}$	−750.
$a_3^{\mathrm{ey,p}}$	−82.0	$a_4^{\mathrm{ey,p}}$	19.0	$a_5^{\mathrm{ey,p}}$	0.0990
$a_6^{\mathrm{ey,p}}$	−17.3	$a_7^{\mathrm{ey,p}}$	−0.995	$a_8^{\mathrm{ey,p}}$	401.4
$a_9^{\mathrm{ey,p}}$	82.0	$a_{10}^{\mathrm{ey,p}}$	750.0	$a_{11}^{\mathrm{ey,p}}$	59.9
$a_{12}^{\mathrm{ey,p}}$	628.0	$a_{13}^{\mathrm{ey,p}}$	0.00679	$a_{14}^{\mathrm{ey,p}}$	−0.628
$a_{15}^{\mathrm{ey,p}}$	−0.0256	$a_{16}^{\mathrm{ey,p}}$	1.18	$a_{17}^{\mathrm{ey,p}}$	−0.000112
$a_{18}^{\mathrm{ey,p}}$	−0.0187	$a_{19}^{\mathrm{ey,p}}$	0.979	$a_{20}^{\mathrm{ey,p}}$	0.0236
$a_{21}^{\mathrm{ey,p}}$	−0.00463	$a_{22}^{\mathrm{ey,p}}$	0.000112	$a_{23}^{\mathrm{ey,p}}$	0.0187
$a_{24}^{\mathrm{ey,p}}$	−1.18	$a_{25}^{\mathrm{ey,p}}$	0.00463	$a_{26}^{\mathrm{ey,p}}$	−0.979
$a_{27}^{\mathrm{ey,p}}$	−0.0236	$a_{28}^{\mathrm{ey,p}}$	0.628	$a_{29}^{\mathrm{ey,p}}$	0.0256
$a_{30}^{\mathrm{ey,p}}$	−0.00679	$a_{31}^{\mathrm{ey,p}}$	0.298	$a_{32}^{\mathrm{ey,p}}$	0.0418
$a_{33}^{\mathrm{ey,p}}$	0.0464	$a_{34}^{\mathrm{ey,p}}$	0.0506	$a_{35}^{\mathrm{ey,p}}$	0.0505
$a_{36}^{\mathrm{ey,p}}$	−0.0131	$a_{37}^{\mathrm{ey,p}}$	−0.0735	$a_{38}^{\mathrm{ey,p}}$	−1.21
$a_{39}^{\mathrm{ey,p}}$	−0.0331	$a_{40}^{\mathrm{ey,p}}$	−0.0155	$a_{41}^{\mathrm{ey,p}}$	−0.0485
$a_{42}^{\mathrm{ey,p}}$	−0.0674				

Appendix A.2. Electrolyzer Temperature Change

$$\gamma^{\mathrm{op,ey}} \cdot a_0^{\mathrm{ey,T}} + a_1^{\mathrm{ey,T}} \cdot i^{\mathrm{ey}} \leq 0 \tag{A33}$$

$$\gamma^{\mathrm{op,ey}} \cdot a_2^{\mathrm{ey,T}} - a_1^{\mathrm{ey,T}} \cdot i^{\mathrm{ey}} \leq 0 \tag{A34}$$

$$\gamma^{\mathrm{op,ey}} \cdot a_3^{\mathrm{ey,T}} - a_1^{\mathrm{ey,T}} \cdot \epsilon T^{\mathrm{ey,on}} \leq 0 \tag{A35}$$

$$\gamma^{\mathrm{op,ey}} \cdot a_4^{\mathrm{ey,T}} + a_1^{\mathrm{ey,T}} \cdot \epsilon T^{\mathrm{ey,on}} \leq 0 \tag{A36}$$

$$\gamma^{\mathrm{op,ey}} \cdot a_6^{\mathrm{ey,T}} + a_5^{\mathrm{ey,T}} \cdot i^{\mathrm{ey}} + a_7^{\mathrm{ey,T}} \cdot \epsilon T^{\mathrm{ey,on}} \leq 0 \tag{A37}$$

$$x_0^{0,\mathrm{ey,T}} \leq a_8^{\mathrm{ey,T}} \cdot \gamma^{0,\mathrm{ey,T}} \tag{A38}$$

$$x_0^{0,\mathrm{ey,T}} \geq 0 \tag{A39}$$

$$x_1^{0,\mathrm{ey,T}} \leq a_9^{\mathrm{ey,T}} \cdot \gamma^{0,\mathrm{ey,T}} \tag{A40}$$

$$x_1^{0,\mathrm{ey,T}} \geq 0 \tag{A41}$$

$$x_0^{1,\mathrm{ey,T}} \leq -a_2^{\mathrm{ey,T}} \cdot \gamma^{1,\mathrm{ey,T}} \tag{A42}$$

$$x_0^{1,\mathrm{ey,T}} \geq 0 \tag{A43}$$

$$x_1^{1,\mathrm{ey,T}} \leq -a_3^{\mathrm{ey,T}} \cdot \gamma^{1,\mathrm{ey,T}} \tag{A44}$$

$$x_1^{1,\mathrm{ey,T}} \geq 0 \tag{A45}$$

$$x_0^{2,\mathrm{ey,T}} \leq a_{12}^{\mathrm{ey,T}} \cdot \gamma^{2,\mathrm{ey,T}} \tag{A46}$$

$$x_0^{2,\mathrm{ey,T}} \geq 0 \tag{A47}$$

$$x_1^{2,\mathrm{ey,T}} \leq -a_3^{\mathrm{ey,T}} \cdot \gamma^{2,\mathrm{ey,T}} \tag{A48}$$

$$x_1^{2,\mathrm{ey,T}} \geq 0 \tag{A49}$$

$$x_0^{3,ey,T} \leq a_{13}^{ey,T} \cdot \gamma^{3,ey,T} \tag{A50}$$

$$x_0^{3,ey,T} \geq 0 \tag{A51}$$

$$x_1^{3,ey,T} \leq a_{14}^{ey,T} \cdot \gamma^{3,ey,T} \tag{A52}$$

$$x_1^{3,ey,T} \geq 0 \tag{A53}$$

$$a_{15}^{ey,T} \cdot x_0^{0,ey,T} + a_{16}^{ey,T} \cdot x_1^{0,ey,T} + a_{17}^{ey,T} \cdot \gamma^{0,ey,T} \leq 0 \tag{A54}$$

$$a_{18}^{ey,T} \cdot \gamma^{0,ey,T} + a_{19}^{ey,T} \cdot x_1^{0,ey,T} + a_{20}^{ey,T} \cdot x_0^{0,ey,T} \leq 0 \tag{A55}$$

$$-a_{17}^{ey,T} \cdot \gamma^{1,ey,T} + a_{22}^{ey,T} \cdot x_0^{1,ey,T} + a_{23}^{ey,T} \cdot x_1^{1,ey,T} \leq 0 \tag{A56}$$

$$a_{18}^{ey,T} \cdot \gamma^{1,ey,T} + a_{19}^{ey,T} \cdot x_1^{1,ey,T} + a_{20}^{ey,T} \cdot x_0^{1,ey,T} \leq 0 \tag{A57}$$

$$a_{24}^{ey,T} \cdot \gamma^{2,ey,T} + a_{25}^{ey,T} \cdot x_0^{2,ey,T} + a_{26}^{ey,T} \cdot x_1^{2,ey,T} \leq 0 \tag{A58}$$

$$-a_{20}^{ey,T} \cdot x_0^{2,ey,T} + a_{28}^{ey,T} \cdot \gamma^{2,ey,T} + a_{29}^{ey,T} \cdot x_1^{2,ey,T} \leq 0 \tag{A59}$$

$$-a_{25}^{ey,T} \cdot x_0^{3,ey,T} - a_{26}^{ey,T} \cdot x_1^{3,ey,T} + a_{32}^{ey,T} \cdot \gamma^{3,ey,T} \leq 0 \tag{A60}$$

$$-a_{20}^{ey,T} \cdot x_0^{3,ey,T} + a_{28}^{ey,T} \cdot \gamma^{3,ey,T} + a_{29}^{ey,T} \cdot x_1^{3,ey,T} \leq 0 \tag{A61}$$

$$\gamma^{0,ey,T} + \gamma^{1,ey,T} + \gamma^{2,ey,T} + \gamma^{3,ey,T} = \gamma^{op,ey} \tag{A62}$$

$$\begin{aligned} \Delta T^{ey,on} = {} & a_{33}^{ey,T} \cdot x_0^{0,ey,T} + a_{34}^{ey,T} \cdot \gamma^{0,ey,T} + a_{35}^{ey,T} \cdot x_0^{3,ey,T} \\ & + a_{36}^{ey,T} \cdot \gamma^{2,ey,T} + a_{37}^{ey,T} \cdot \gamma^{1,ey,T} + a_{38}^{ey,T} \cdot \gamma^{3,ey,T} \\ & + a_{39}^{ey,T} \cdot x_0^{2,ey,T} + a_{40}^{ey,T} \cdot x_0^{1,ey,T} + a_{41}^{ey,T} \cdot x_1^{3,ey,T} \\ & + a_{42}^{ey,T} \cdot x_1^{0,ey,T} + a_{43}^{ey,T} \cdot x_1^{1,ey,T} + a_{44}^{ey,T} \cdot x_1^{2,ey,T} \end{aligned} \tag{A63}$$

$$i^{ey} = x_0^{0,ey,T} + x_0^{1,ey,T} + x_0^{2,ey,T} + x_0^{3,ey,T} \tag{A64}$$

$$\epsilon T^{ey,on} = x_1^{0,ey,T} + x_1^{1,ey,T} + x_1^{2,ey,T} + x_1^{3,ey,T} \tag{A65}$$

Table A2. Constants for the piecewise linear model of the temperature changes of the electrolyzer.

Constant	Value	Constant	Value	Constant	Value
$a_0^{ey,T}$	135.0	$a_1^{ey,T}$	−1.00	$a_2^{ey,T}$	−750.
$a_3^{ey,T}$	−82.0	$a_4^{ey,T}$	19.0	$a_5^{ey,T}$	0.0990
$a_6^{ey,T}$	−17.3	$a_7^{ey,T}$	−0.995	$a_8^{ey,T}$	683.1
$a_9^{ey,T}$	55.9	$a_{10}^{ey,T}$	750.0	$a_{11}^{ey,T}$	82.0
$a_{12}^{ey,T}$	574.6	$a_{13}^{ey,T}$	373.8	$a_{14}^{ey,T}$	74.1
$a_{15}^{ey,T}$	0.000812	$a_{16}^{ey,T}$	0.0424	$a_{17}^{ey,T}$	−2.70
$a_{18}^{ey,T}$	0.339	$a_{19}^{ey,T}$	0.0547	$a_{20}^{ey,T}$	−0.00839
$a_{21}^{ey,T}$	2.70	$a_{22}^{ey,T}$	−0.000812	$a_{23}^{ey,T}$	−0.0424
$a_{24}^{ey,T}$	1.88	$a_{25}^{ey,T}$	−0.00208	$a_{26}^{ey,T}$	−0.0216
$a_{27}^{ey,T}$	0.00839	$a_{28}^{ey,T}$	−0.339	$a_{29}^{ey,T}$	−0.0547
$a_{30}^{ey,T}$	0.00208	$a_{31}^{ey,T}$	0.0216	$a_{32}^{ey,T}$	−1.88
$a_{33}^{ey,T}$	0.0158	$a_{34}^{ey,T}$	0.447	$a_{35}^{ey,T}$	0.00919

Table A2. *Cont.*

Constant	Value	Constant	Value	Constant	Value
$a_{36}^{\mathrm{ey,T}}$	2.72	$a_{37}^{\mathrm{ey,T}}$	3.24	$a_{38}^{\mathrm{ey,T}}$	0.809
$a_{39}^{\mathrm{ey,T}}$	0.00721	$a_{40}^{\mathrm{ey,T}}$	0.0149	$a_{41}^{\mathrm{ey,T}}$	−0.0437
$a_{42}^{\mathrm{ey,T}}$	−0.0842	$a_{43}^{\mathrm{ey,T}}$	−0.127	$a_{44}^{\mathrm{ey,T}}$	−0.0660

Appendix A.3. Fuel Cell Power

$$\gamma^{\mathrm{op,fc}} \cdot a_0^{\mathrm{fc}} + a_1^{\mathrm{fc}} \cdot \epsilon U^{\mathrm{bus}} \leq 0 \tag{A66}$$

$$\gamma^{\mathrm{op,fc}} \cdot a_2^{\mathrm{fc}} + a_1^{\mathrm{fc}} \cdot i^{\mathrm{fc}} \leq 0 \tag{A67}$$

$$\gamma^{\mathrm{op,fc}} \cdot a_3^{\mathrm{fc}} - a_1^{\mathrm{fc}} \cdot i^{\mathrm{fc}} \leq 0 \tag{A68}$$

$$\gamma^{\mathrm{op,fc}} \cdot a_4^{\mathrm{fc}} - a_1^{\mathrm{fc}} \cdot \epsilon U^{\mathrm{bus}} \leq 0 \tag{A69}$$

$$x_0^{0,\mathrm{fc}} \leq -a_3^{\mathrm{fc}} \cdot \gamma^{0,\mathrm{fc}} \tag{A70}$$

$$x_0^{0,\mathrm{fc}} \geq 0 \tag{A71}$$

$$x_1^{0,\mathrm{fc}} \leq -a_4^{\mathrm{fc}} \cdot \gamma^{0,\mathrm{fc}} \tag{A72}$$

$$x_1^{0,\mathrm{fc}} \geq 0 \tag{A73}$$

$$x_0^{1,\mathrm{fc}} \leq a_6^{\mathrm{fc}} \cdot \gamma^{1,\mathrm{fc}} \tag{A74}$$

$$x_0^{1,\mathrm{fc}} \geq 0 \tag{A75}$$

$$x_1^{1,\mathrm{fc}} \leq -a_4^{\mathrm{fc}} \cdot \gamma^{1,\mathrm{fc}} \tag{A76}$$

$$x_1^{1,\mathrm{fc}} \geq 0 \tag{A77}$$

$$x_0^{2,\mathrm{fc}} \leq a_7^{\mathrm{fc}} \cdot \gamma^{2,\mathrm{fc}} \tag{A78}$$

$$x_0^{2,\mathrm{fc}} \geq 0 \tag{A79}$$

$$x_1^{2,\mathrm{fc}} \leq -a_4^{\mathrm{fc}} \cdot \gamma^{2,\mathrm{fc}} \tag{A80}$$

$$x_1^{2,\mathrm{fc}} \geq 0 \tag{A81}$$

$$a_{10}^{\mathrm{fc}} \cdot x_0^{0,\mathrm{fc}} + a_8^{\mathrm{fc}} \cdot \gamma^{0,\mathrm{fc}} + a_9^{\mathrm{fc}} \cdot x_1^{0,\mathrm{fc}} \leq 0 \tag{A82}$$

$$-a_{10}^{\mathrm{fc}} \cdot x_0^{1,\mathrm{fc}} + a_{12}^{\mathrm{fc}} \cdot \gamma^{1,\mathrm{fc}} + a_{13}^{\mathrm{fc}} \cdot x_1^{1,\mathrm{fc}} \leq 0 \tag{A83}$$

$$a_{14}^{\mathrm{fc}} \cdot \gamma^{1,\mathrm{fc}} + a_{15}^{\mathrm{fc}} \cdot x_1^{1,\mathrm{fc}} + a_{16}^{\mathrm{fc}} \cdot x_0^{1,\mathrm{fc}} \leq 0 \tag{A84}$$

$$-a_{16}^{\mathrm{fc}} \cdot x_0^{2,\mathrm{fc}} + a_{18}^{\mathrm{fc}} \cdot \gamma^{2,\mathrm{fc}} + a_{19}^{\mathrm{fc}} \cdot x_1^{2,\mathrm{fc}} \leq 0 \tag{A85}$$

$$\gamma^{0,\mathrm{fc}} + \gamma^{1,\mathrm{fc}} + \gamma^{2,\mathrm{fc}} = \gamma^{\mathrm{op,fc}} \tag{A86}$$

$$\begin{aligned} p^{\mathrm{fc}} = {} & a_{20}^{\mathrm{fc}} \cdot \gamma^{2,\mathrm{fc}} + a_{21}^{\mathrm{fc}} \cdot \gamma^{1,\mathrm{fc}} + a_{22}^{\mathrm{fc}} \cdot \gamma^{0,\mathrm{fc}} + \\ & a_{23}^{\mathrm{fc}} \cdot x_0^{2,\mathrm{fc}} + a_{24}^{\mathrm{fc}} \cdot x_1^{1,\mathrm{fc}} + a_{25}^{\mathrm{fc}} \cdot x_0^{1,\mathrm{fc}} + a_{26}^{\mathrm{fc}} \cdot x_1^{2,\mathrm{fc}} + \\ & a_{27}^{\mathrm{fc}} \cdot x_0^{0,\mathrm{fc}} + a_{28}^{\mathrm{fc}} \cdot x_1^{0,\mathrm{fc}} \end{aligned} \tag{A87}$$

$$i^{\mathrm{fc}} = x_0^{0,\mathrm{fc}} + x_0^{1,\mathrm{fc}} + x_0^{2,\mathrm{fc}} \tag{A88}$$

$$\epsilon U^{\mathrm{bus}} = x_1^{0,\mathrm{fc}} + x_1^{1,\mathrm{fc}} + x_1^{2,\mathrm{fc}} \tag{A89}$$

Table A3. Constants for the piecewise linear model of the power output of the fuel cell.

Constant	Value	Constant	Value	Constant	Value
a_0^{fc}	200.0	a_1^{fc}	-1.00	a_2^{fc}	20.0
a_3^{fc}	-200	a_4^{fc}	$-260.$	a_5^{fc}	260.0
a_6^{fc}	153.3	a_7^{fc}	95.0	a_8^{fc}	1.14
a_9^{fc}	0.000373	a_{10}^{fc}	-0.00808	a_{11}^{fc}	0.00808
a_{12}^{fc}	-1.14	a_{13}^{fc}	-0.000373	a_{14}^{fc}	1.08
a_{15}^{fc}	0.00108	a_{16}^{fc}	-0.0143	a_{17}^{fc}	0.0143
a_{18}^{fc}	-1.08	a_{19}^{fc}	-0.00108	a_{20}^{fc}	0.0945
a_{21}^{fc}	0.857	a_{22}^{fc}	1.98	a_{23}^{fc}	0.0325
a_{24}^{fc}	0.00153	a_{25}^{fc}	0.0219	a_{26}^{fc}	0.000725
a_{27}^{fc}	0.0139	a_{28}^{fc}	0.00192		

Appendix A.4. Battery Voltage

$$1 \cdot a_1^{\text{bat}} + a_0^{\text{bat}} \cdot p^{\text{bat}} + a_2^{\text{bat}} \cdot soc \leq 0 \tag{A90}$$

$$1 \cdot a_4^{\text{bat}} + a_3^{\text{bat}} \cdot p^{\text{bat}} + 1.0 \cdot soc \leq 0 \tag{A91}$$

$$1 \cdot a_5^{\text{bat}} + a_6^{\text{bat}} \cdot soc \leq 0 \tag{A92}$$

$$1 \cdot a_8^{\text{bat}} + a_7^{\text{bat}} \cdot p^{\text{bat}} + a_9^{\text{bat}} \cdot soc \leq 0 \tag{A93}$$

$$x_0^{0,\text{bat}} \leq a_{10}^{\text{bat}} \cdot \gamma^{0,\text{bat}} \tag{A94}$$

$$x_0^{0,\text{bat}} \geq 0 \tag{A95}$$

$$x_1^{0,\text{bat}} \leq a_{11}^{\text{bat}} \cdot \gamma^{0,\text{bat}} \tag{A96}$$

$$x_1^{0,\text{bat}} \geq a_{12}^{\text{bat}} \cdot \gamma^{0,\text{bat}} \tag{A97}$$

$$x_0^{1,\text{bat}} \leq a_{13}^{\text{bat}} \cdot \gamma^{1,\text{bat}} \tag{A98}$$

$$x_0^{1,\text{bat}} \geq 0 \tag{A99}$$

$$x_1^{1,\text{bat}} \leq a_{14}^{\text{bat}} \cdot \gamma^{1,\text{bat}} \tag{A100}$$

$$x_1^{1,\text{bat}} \geq 0 \tag{A101}$$

$$x_0^{2,\text{bat}} \leq a_{15}^{\text{bat}} \cdot \gamma^{2,\text{bat}} \tag{A102}$$

$$x_0^{2,\text{bat}} \geq 0 \tag{A103}$$

$$x_1^{2,\text{bat}} \leq a_{16}^{\text{bat}} \cdot \gamma^{2,\text{bat}} \tag{A104}$$

$$x_1^{2,\text{bat}} \geq a_{17}^{\text{bat}} \cdot \gamma^{2,\text{bat}} \tag{A105}$$

$$x_0^{3,\text{bat}} \leq a_{18}^{\text{bat}} \cdot \gamma^{3,\text{bat}} \tag{A106}$$

$$x_0^{3,\text{bat}} \geq 0 \tag{A107}$$

$$x_1^{3,\text{bat}} \leq a_{19}^{\text{bat}} \cdot \gamma^{3,\text{bat}} \tag{A108}$$

$$x_1^{3,\text{bat}} \geq a_{20}^{\text{bat}} \cdot \gamma^{3,\text{bat}} \tag{A109}$$

$$a_{21}^{\text{bat}} \cdot x_1^{0,\text{bat}} + a_{22}^{\text{bat}} \cdot \gamma^{0,\text{bat}} + a_{23}^{\text{bat}} \cdot x_0^{0,\text{bat}} \leq 0 \tag{A110}$$

$$a_{24}^{\text{bat}} \cdot \gamma^{0,\text{bat}} + a_{25}^{\text{bat}} \cdot x_0^{0,\text{bat}} + a_{26}^{\text{bat}} \cdot x_1^{0,\text{bat}} \leq 0 \tag{A111}$$

$$a_{27}^{\text{bat}} \cdot \gamma^{0,\text{bat}} + a_{28}^{\text{bat}} \cdot x_1^{0,\text{bat}} + a_{29}^{\text{bat}} \cdot x_0^{0,\text{bat}} \leq 0 \tag{A112}$$

$$-a_{22}^{\text{bat}} \cdot \gamma^{1,\text{bat}} - a_{23}^{\text{bat}} \cdot x_0^{1,\text{bat}} + a_{32}^{\text{bat}} \cdot x_1^{1,\text{bat}} \leq 0 \tag{A113}$$

$$a_{24}^{\text{bat}} \cdot \gamma^{1,\text{bat}} + a_{25}^{\text{bat}} \cdot x_0^{1,\text{bat}} + a_{26}^{\text{bat}} \cdot x_1^{1,\text{bat}} \leq 0 \tag{A114}$$

$$-a_{25}^{\text{bat}} \cdot x_0^{2,\text{bat}} - a_{26}^{\text{bat}} \cdot x_1^{2,\text{bat}} + a_{35}^{\text{bat}} \cdot \gamma^{2,\text{bat}} \leq 0 \tag{A115}$$

$$a_{27}^{\text{bat}} \cdot \gamma^{2,\text{bat}} + a_{28}^{\text{bat}} \cdot x_1^{2,\text{bat}} + a_{29}^{\text{bat}} \cdot x_0^{2,\text{bat}} \leq 0 \tag{A116}$$

$$-a_{28}^{\text{bat}} \cdot x_1^{3,\text{bat}} - a_{29}^{\text{bat}} \cdot x_0^{3,\text{bat}} + a_{38}^{\text{bat}} \cdot \gamma^{3,\text{bat}} \leq 0 \tag{A117}$$

$$\gamma^{0,\text{bat}} + \gamma^{1,\text{bat}} + \gamma^{2,\text{bat}} + \gamma^{3,\text{bat}} = 1 \tag{A118}$$

$$\begin{aligned} U^{\text{bat}} = a_{39}^{\text{bat}} \cdot x_1^{2,\text{bat}} + a_{40}^{\text{bat}} \cdot x_1^{1,\text{bat}} + a_{41}^{\text{bat}} \cdot \gamma^{0,\text{bat}} \\ + a_{42}^{\text{bat}} \cdot x_0^{1,\text{bat}} + a_{43}^{\text{bat}} \cdot x_0^{3,\text{bat}} \\ + a_{44}^{\text{bat}} \cdot x_1^{3,\text{bat}} + a_{45}^{\text{bat}} \cdot x_1^{0,\text{bat}} \\ + a_{46}^{\text{bat}} \cdot \gamma^{1,\text{bat}} + a_{47}^{\text{bat}} \cdot x_0^{0,\text{bat}} \\ + a_{48}^{\text{bat}} \cdot \gamma^{3,\text{bat}} + a_{49}^{\text{bat}} \cdot \gamma^{2,\text{bat}} \\ + a_{50}^{\text{bat}} \cdot x_0^{2,\text{bat}} \end{aligned} \tag{A119}$$

$$soc = x_0^{0,\text{bat}} + x_0^{1,\text{bat}} + x_0^{2,\text{bat}} + x_0^{3,\text{bat}} \tag{A120}$$

$$p^{\text{bat}} = x_1^{0,\text{bat}} + x_1^{1,\text{bat}} + x_1^{2,\text{bat}} + x_1^{3,\text{bat}} \tag{A121}$$

Table A4. Constants for the piecewise linear model for the voltage of the battery.

Constant	Value	Constant	Value	Constant	Value
a_0^{bat}	-0.659	a_1^{bat}	-11.4	a_2^{bat}	-0.752
a_3^{bat}	1.18×10^{-16}	a_4^{bat}	-0.990	a_5^{bat}	0.200
a_6^{bat}	-1.00	a_7^{bat}	0.341	a_8^{bat}	-6.29
a_9^{bat}	-0.940	a_{10}^{bat}	0.990	a_{11}^{bat}	5.22
a_{12}^{bat}	-5.58	a_{13}^{bat}	0.990	a_{14}^{bat}	21.2
a_{15}^{bat}	0.879	a_{16}^{bat}	19.7	a_{17}^{bat}	-4.29
a_{18}^{bat}	0.990	a_{19}^{bat}	3.59	a_{20}^{bat}	-18.4
a_{21}^{bat}	2.19	a_{22}^{bat}	-2.01	a_{23}^{bat}	-9.50
a_{24}^{bat}	24.8	a_{25}^{bat}	-31.0	a_{26}^{bat}	-0.577
a_{27}^{bat}	5.32	a_{28}^{bat}	-0.900	a_{29}^{bat}	-10.4
a_{30}^{bat}	2.01	a_{31}^{bat}	9.50	a_{32}^{bat}	-2.19
a_{33}^{bat}	31.0	a_{34}^{bat}	0.577	a_{35}^{bat}	-24.8
a_{36}^{bat}	0.900	a_{37}^{bat}	10.4	a_{38}^{bat}	-5.32
a_{39}^{bat}	0.866	a_{40}^{bat}	0.667	a_{41}^{bat}	198.6
a_{42}^{bat}	52.0	a_{43}^{bat}	13.7	a_{44}^{bat}	0.316
a_{45}^{bat}	2.85	a_{46}^{bat}	200.7	a_{47}^{bat}	42.5
a_{48}^{bat}	220.8	a_{49}^{bat}	221.7	a_{50}^{bat}	14.0

Appendix A.5. Battery Current

$$1 \cdot a_1^{\text{bat,i}} + a_0^{\text{bat,i}} \cdot p^{\text{bat}} + a_2^{\text{bat,i}} \cdot soc \leq 0 \tag{A122}$$

$$1 \cdot a_4^{\text{bat,i}} + a_3^{\text{bat,i}} \cdot p^{\text{bat}} + 1.0 \cdot soc \leq 0 \tag{A123}$$

$$1 \cdot a_5^{\text{bat,i}} + a_6^{\text{bat,i}} \cdot soc \leq 0 \tag{A124}$$

$$1 \cdot a_8^{\text{bat,i}} + a_7^{\text{bat,i}} \cdot p^{\text{bat}} + a_9^{\text{bat,i}} \cdot soc \leq 0 \tag{A125}$$

$$x_0^{0,\text{bat,i}} \leq a_{10}^{\text{bat,i}} \cdot \gamma^{0,\text{bat,i}} \tag{A126}$$

$$x_0^{0,\text{bat,i}} \geq 0 \tag{A127}$$

$$x_1^{0,\text{bat,i}} \leq a_{11}^{\text{bat,i}} \cdot \gamma^{0,\text{bat,i}} \tag{A128}$$

$$x_1^{0,\text{bat,i}} \geq a_{12}^{\text{bat,i}} \cdot \gamma^{0,\text{bat,i}} \tag{A129}$$

$$x_0^{1,\text{bat,i}} \leq a_{10}^{\text{bat,i}} \cdot \gamma^{1,\text{bat,i}} \tag{A130}$$

$$x_0^{1,\text{bat,i}} \geq 0 \tag{A131}$$

$$x_1^{1,\text{bat,i}} \leq a_{13}^{\text{bat,i}} \cdot \gamma^{1,\text{bat,i}} \tag{A132}$$

$$x_1^{1,\text{bat,i}} \geq a_{14}^{\text{bat,i}} \cdot \gamma^{1,\text{bat,i}} \tag{A133}$$

$$x_0^{2,\text{bat,i}} \leq a_{15}^{\text{bat,i}} \cdot \gamma^{2,\text{bat,i}} \tag{A134}$$

$$x_0^{2,\text{bat,i}} \geq 0 \tag{A135}$$

$$x_1^{2,\text{bat,i}} \leq a_{16}^{\text{bat,i}} \cdot \gamma^{2,\text{bat,i}} \tag{A136}$$

$$x_1^{2,\text{bat,i}} \geq a_{17}^{\text{bat,i}} \cdot \gamma^{2,\text{bat,i}} \tag{A137}$$

$$x_0^{3,\text{bat,i}} \leq a_{18}^{\text{bat,i}} \cdot \gamma^{3,\text{bat,i}} \tag{A138}$$

$$x_0^{3,\text{bat,i}} \geq 0 \tag{A139}$$

$$x_1^{3,\text{bat,i}} \leq a_{19}^{\text{bat,i}} \cdot \gamma^{3,\text{bat,i}} \tag{A140}$$

$$x_1^{3,\text{bat,i}} \geq a_{20}^{\text{bat,i}} \cdot \gamma^{3,\text{bat,i}} \tag{A141}$$

$$a_{21}^{\text{bat,i}} \cdot \gamma^{0,\text{bat,i}} + a_{22}^{\text{bat,i}} \cdot x_1^{0,\text{bat,i}} + a_{23}^{\text{bat,i}} \cdot x_0^{0,\text{bat,i}} \leq 0 \tag{A142}$$

$$-a_{22}^{\text{bat,i}} \cdot x_1^{1,\text{bat,i}} - a_{23}^{\text{bat,i}} \cdot x_0^{1,\text{bat,i}} + a_{26}^{\text{bat,i}} \cdot \gamma^{1,\text{bat,i}} \leq 0 \tag{A143}$$

$$a_{27}^{\text{bat,i}} \cdot \gamma^{1,\text{bat,i}} + a_{28}^{\text{bat,i}} \cdot x_0^{1,\text{bat,i}} + a_{29}^{\text{bat,i}} \cdot x_1^{1,\text{bat,i}} \leq 0 \tag{A144}$$

$$-a_{28}^{\text{bat,i}} \cdot x_0^{2,\text{bat,i}} - a_{29}^{\text{bat,i}} \cdot x_1^{2,\text{bat,i}} + a_{32}^{\text{bat,i}} \cdot \gamma^{2,\text{bat,i}} \leq 0 \tag{A145}$$

$$a_{33}^{\text{bat,i}} \cdot \gamma^{2,\text{bat,i}} + a_{34}^{\text{bat,i}} \cdot x_1^{2,\text{bat,i}} + a_{35}^{\text{bat,i}} \cdot x_0^{2,\text{bat,i}} \leq 0 \tag{A146}$$

$$-a_{34}^{\text{bat,i}} \cdot x_1^{3,\text{bat,i}} - a_{35}^{\text{bat,i}} \cdot x_0^{3,\text{bat,i}} + a_{38}^{\text{bat,i}} \cdot \gamma^{3,\text{bat,i}} \leq 0 \tag{A147}$$

$$\gamma^{0,\text{bat,i}} + \gamma^{1,\text{bat,i}} + \gamma^{2,\text{bat,i}} + \gamma^{3,\text{bat,i}} = 1 \tag{A148}$$

$$\begin{aligned} i^{\text{bat}} = {} & a_{39}^{\text{bat,i}} \cdot x_0^{3,\text{bat,i}} + a_{40}^{\text{bat,i}} \cdot \gamma^{0,\text{bat,i}} + \\ & a_{41}^{\text{bat,i}} \cdot \gamma^{1,\text{bat,i}} + a_{42}^{\text{bat,i}} \cdot \gamma^{2,\text{bat,i}} + \\ & a_{43}^{\text{bat,i}} \cdot x_1^{0,\text{bat,i}} + a_{44}^{\text{bat,i}} \cdot x_1^{2,\text{bat,i}} + \\ & a_{45}^{\text{bat,i}} \cdot x_1^{3,\text{bat,i}} + a_{46}^{\text{bat,i}} \cdot x_1^{1,\text{bat,i}} + \\ & a_{47}^{\text{bat,i}} \cdot \gamma^{3,\text{bat,i}} + a_{48}^{\text{bat,i}} \cdot x_0^{0,\text{bat,i}} + \\ & a_{49}^{\text{bat,i}} \cdot x_0^{2,\text{bat,i}} + a_{50}^{\text{bat,i}} \cdot x_0^{1,\text{bat,i}} \end{aligned} \tag{A149}$$

$$soc = x_0^{0,\text{bat,i}} + x_0^{1,\text{bat,i}} + x_0^{2,\text{bat,i}} + x_0^{3,\text{bat,i}} \tag{A150}$$

$$p^{\text{bat}} = x_1^{0,\text{bat,i}} + x_1^{1,\text{bat,i}} + x_1^{2,\text{bat,i}} + x_1^{3,\text{bat,i}} \tag{A151}$$

Table A5. Constants for the piecewise linear model of the current of the battery.

Constant	Value	Constant	Value	Constant	Value
$a_0^{\text{bat,i}}$	-0.659	$a_1^{\text{bat,i}}$	-11.4	$a_2^{\text{bat,i}}$	-0.752
$a_3^{\text{bat,i}}$	1.18×10^{-16}	$a_4^{\text{bat,i}}$	-0.990	$a_5^{\text{bat,i}}$	0.200
$a_6^{\text{bat,i}}$	-1.00	$a_7^{\text{bat,i}}$	0.341	$a_8^{\text{bat,i}}$	-6.29
$a_9^{\text{bat,i}}$	-0.940	$a_{10}^{\text{bat,i}}$	0.990	$a_{11}^{\text{bat,i}}$	21.2
$a_{12}^{\text{bat,i}}$	-0.111	$a_{13}^{\text{bat,i}}$	19.9	$a_{14}^{\text{bat,i}}$	-0.483
$a_{15}^{\text{bat,i}}$	0.990	$a_{16}^{\text{bat,i}}$	19.5	$a_{17}^{\text{bat,i}}$	-2.73
$a_{18}^{\text{bat,i}}$	0.990	$a_{19}^{\text{bat,i}}$	8.16	$a_{20}^{\text{bat,i}}$	-18.4
$a_{21}^{\text{bat,i}}$	10.3	$a_{22}^{\text{bat,i}}$	-0.241	$a_{23}^{\text{bat,i}}$	-10.5
$a_{24}^{\text{bat,i}}$	0.241	$a_{25}^{\text{bat,i}}$	10.5	$a_{26}^{\text{bat,i}}$	-10.3
$a_{27}^{\text{bat,i}}$	10.9	$a_{28}^{\text{bat,i}}$	-11.2	$a_{29}^{\text{bat,i}}$	-0.354
$a_{30}^{\text{bat,i}}$	11.2	$a_{31}^{\text{bat,i}}$	0.354	$a_{32}^{\text{bat,i}}$	-10.9
$a_{33}^{\text{bat,i}}$	5.66	$a_{34}^{\text{bat,i}}$	-0.519	$a_{35}^{\text{bat,i}}$	-7.15
$a_{36}^{\text{bat,i}}$	0.519	$a_{37}^{\text{bat,i}}$	7.15	$a_{38}^{\text{bat,i}}$	-5.66
$a_{39}^{\text{bat,i}}$	1.12	$a_{40}^{\text{bat,i}}$	15.8	$a_{41}^{\text{bat,i}}$	5.37
$a_{42}^{\text{bat,i}}$	1.73	$a_{43}^{\text{bat,i}}$	3.75	$a_{44}^{\text{bat,i}}$	4.12
$a_{45}^{\text{bat,i}}$	4.45	$a_{46}^{\text{bat,i}}$	3.99	$a_{47}^{\text{bat,i}}$	-0.597
$a_{48}^{\text{bat,i}}$	-16.4	$a_{49}^{\text{bat,i}}$	-2.10	$a_{50}^{\text{bat,i}}$	-5.90

Appendix A.6. Compressor

$$\gamma^{\text{op,comp}} \cdot a_0^{\text{comp}} + a_1^{\text{comp}} \cdot n^{\text{H2,comp}} \leq 0 \tag{A152}$$

$$\gamma^{\text{op,comp}} \cdot a_0^{\text{comp}} + a_1^{\text{comp}} \cdot n^{\text{H2,comp}} \leq 0 \tag{A153}$$

$$\gamma^{\text{op,comp}} \cdot a_2^{\text{comp}} + a_1^{\text{comp}} \cdot \epsilon pr^{\text{comp,out}} \leq 0 \tag{A154}$$

$$\gamma^{\text{op,comp}} \cdot a_2^{\text{comp}} + a_1^{\text{comp}} \cdot \epsilon pr^{\text{comp,out}} \leq 0 \tag{A155}$$

$$\gamma^{\text{op,comp}} \cdot a_3^{\text{comp}} - a_1^{\text{comp}} \cdot \epsilon pr^{\text{comp,in}} \leq 0 \tag{A156}$$

$$\gamma^{\text{op,comp}} \cdot a_3^{\text{comp}} - a_1^{\text{comp}} \cdot \epsilon pr^{\text{comp,in}} \leq 0 \tag{A157}$$

$$\gamma^{\text{op,comp}} \cdot a_4^{\text{comp}} - a_1^{\text{comp}} \cdot n^{\text{H2,comp}} \leq 0 \tag{A158}$$

$$\gamma^{\text{op,comp}} \cdot a_4^{\text{comp}} - a_1^{\text{comp}} \cdot n^{\text{H2,comp}} \leq 0 \tag{A159}$$

$$\gamma^{\text{op,comp}} \cdot a_5^{\text{comp}} - a_1^{\text{comp}} \cdot \epsilon pr^{\text{comp,out}} \leq 0 \tag{A160}$$

$$\gamma^{\text{op,comp}} \cdot a_5^{\text{comp}} - a_1^{\text{comp}} \cdot \epsilon pr^{\text{comp,out}} \leq 0 \tag{A161}$$

$$\gamma^{\text{op,comp}} \cdot a_6^{\text{comp}} + a_1^{\text{comp}} \cdot \epsilon pr^{\text{comp,in}} \leq 0 \tag{A162}$$

$$\gamma^{\text{op,comp}} \cdot a_6^{\text{comp}} + a_1^{\text{comp}} \cdot \epsilon pr^{\text{comp,in}} \leq 0 \tag{A163}$$

$$x_0^{0,\text{comp}} \leq a_7^{\text{comp}} \cdot \gamma^{0,\text{comp}} \tag{A164}$$

$$x_0^{0,\text{comp}} \geq 0 \tag{A165}$$

$$x_1^{0,\text{comp}} \leq a_8^{\text{comp}} \cdot \gamma^{0,\text{comp}} \tag{A166}$$

$$x_1^{0,\text{comp}} \geq 0 \tag{A167}$$

$$x_2^{0,\text{comp}} \leq a_9^{\text{comp}} \cdot \gamma^{0,\text{comp}} \tag{A168}$$

$$x_2^{0,\text{comp}} \geq 0 \tag{A169}$$

$$x_0^{1,\text{comp}} \leq -a_3^{\text{comp}} \cdot \gamma^{1,\text{comp}} \tag{A170}$$

$$x_0^{1,\text{comp}} \geq 0 \tag{A171}$$

$$x_1^{1,\text{comp}} \leq a_{11}^{\text{comp}} \cdot \gamma^{1,\text{comp}} \tag{A172}$$

$$x_1^{1,\text{comp}} \geq 0 \tag{A173}$$

$$x_2^{1,\text{comp}} \leq a_{12}^{\text{comp}} \cdot \gamma^{1,\text{comp}} \tag{A174}$$

$$x_2^{1,\text{comp}} \geq 0 \tag{A175}$$

$$x_0^{2,\text{comp}} \leq a_{13}^{\text{comp}} \cdot \gamma^{2,\text{comp}} \tag{A176}$$

$$x_0^{2,\text{comp}} \geq 0 \tag{A177}$$

$$x_1^{2,\text{comp}} \leq a_{14}^{\text{comp}} \cdot \gamma^{2,\text{comp}} \tag{A178}$$

$$x_1^{2,\text{comp}} \geq 0 \tag{A179}$$

$$x_2^{2,\text{comp}} \leq a_{12}^{\text{comp}} \cdot \gamma^{2,\text{comp}} \tag{A180}$$

$$x_2^{2,\text{comp}} \geq 0 \tag{A181}$$

$$x_0^{3,\text{comp}} \leq a_{15}^{\text{comp}} \cdot \gamma^{3,\text{comp}} \tag{A182}$$

$$x_0^{3,\text{comp}} \geq 0 \tag{A183}$$

$$x_1^{3,\text{comp}} \leq a_{16}^{\text{comp}} \cdot \gamma^{3,\text{comp}} \tag{A184}$$

$$x_1^{3,\text{comp}} \geq 0 \tag{A185}$$

$$x_2^{3,\text{comp}} \leq a_{17}^{\text{comp}} \cdot \gamma^{3,\text{comp}} \tag{A186}$$

$$x_2^{3,\text{comp}} \geq 0 \tag{A187}$$

$$x_0^{4,\text{comp}} \leq a_{18}^{\text{comp}} \cdot \gamma^{4,\text{comp}} \tag{A188}$$

$$x_0^{4,\text{comp}} \geq 0 \tag{A189}$$

$$x_1^{4,\text{comp}} \leq a_{19}^{\text{comp}} \cdot \gamma^{4,\text{comp}} \tag{A190}$$

$$x_1^{4,\text{comp}} \geq 0 \tag{A191}$$

$$x_2^{4,\text{comp}} \leq a_{12}^{\text{comp}} \cdot \gamma^{4,\text{comp}} \tag{A192}$$

$$x_2^{4,\text{comp}} \geq 0 \tag{A193}$$

$$a_{20}^{\text{comp}} \cdot \gamma^{0,\text{comp}} + a_{21}^{\text{comp}} \cdot x_0^{0,\text{comp}} + a_{22}^{\text{comp}} \cdot x_1^{0,\text{comp}} + a_{23}^{\text{comp}} \cdot x_2^{0,\text{comp}} \leq 0 \tag{A194}$$

$$a_{24}^{\text{comp}} \cdot x_0^{0,\text{comp}} + a_{25}^{\text{comp}} \cdot x_2^{0,\text{comp}} + a_{26}^{\text{comp}} \cdot \gamma^{0,\text{comp}} + a_{27}^{\text{comp}} \cdot x_1^{0,\text{comp}} \leq 0 \tag{A195}$$

$$-a_{22}^{\text{comp}} \cdot x_1^{1,\text{comp}} - a_{23}^{\text{comp}} \cdot x_2^{1,\text{comp}} + a_{30}^{\text{comp}} \cdot \gamma^{1,\text{comp}} + a_{31}^{\text{comp}} \cdot x_0^{1,\text{comp}} \leq 0 \tag{A196}$$

$$a_{24}^{\text{comp}} \cdot x_0^{1,\text{comp}} + a_{25}^{\text{comp}} \cdot x_2^{1,\text{comp}} + a_{26}^{\text{comp}} \cdot \gamma^{1,\text{comp}} + a_{27}^{\text{comp}} \cdot x_1^{1,\text{comp}} \leq 0 \tag{A197}$$

$$a_{32}^{\text{comp}} \cdot x_1^{2,\text{comp}} + a_{33}^{\text{comp}} \cdot x_2^{2,\text{comp}} + a_{34}^{\text{comp}} \cdot \gamma^{2,\text{comp}} + a_{35}^{\text{comp}} \cdot x_0^{2,\text{comp}} \leq 0 \tag{A198}$$

$$-a_{26}^{\text{comp}} \cdot \gamma^{2,\text{comp}} - a_{27}^{\text{comp}} \cdot x_1^{2,\text{comp}} + a_{38}^{\text{comp}} \cdot x_0^{2,\text{comp}} + a_{39}^{\text{comp}} \cdot x_2^{2,\text{comp}} \leq 0 \tag{A199}$$

$$a_{40}^{\text{comp}} \cdot x_2^{3,\text{comp}} + a_{41}^{\text{comp}} \cdot \gamma^{3,\text{comp}} + a_{42}^{\text{comp}} \cdot x_0^{3,\text{comp}} + a_{43}^{\text{comp}} \cdot x_1^{3,\text{comp}} \leq 0 \tag{A200}$$

$$-a_{34}^{\text{comp}} \cdot \gamma^{3,\text{comp}} - a_{35}^{\text{comp}} \cdot x_0^{3,\text{comp}} + a_{46}^{\text{comp}} \cdot x_1^{3,\text{comp}} + a_{47}^{\text{comp}} \cdot x_2^{3,\text{comp}} \leq 0 \tag{A201}$$

$$-a_{26}^{\text{comp}} \cdot \gamma^{3,\text{comp}} - a_{27}^{\text{comp}} \cdot x_1^{3,\text{comp}} + a_{38}^{\text{comp}} \cdot x_0^{3,\text{comp}} + a_{39}^{\text{comp}} \cdot x_2^{3,\text{comp}} \leq 0 \tag{A202}$$

$$-a_{41}^{\text{comp}} \cdot \gamma^{4,\text{comp}} - a_{42}^{\text{comp}} \cdot x_0^{4,\text{comp}} - a_{43}^{\text{comp}} \cdot x_1^{4,\text{comp}} + a_{51}^{\text{comp}} \cdot x_2^{4,\text{comp}} \leq 0 \tag{A203}$$

$$-a_{34}^{\text{comp}} \cdot \gamma^{4,\text{comp}} - a_{35}^{\text{comp}} \cdot x_0^{4,\text{comp}} + a_{46}^{\text{comp}} \cdot x_1^{4,\text{comp}} + a_{47}^{\text{comp}} \cdot x_2^{4,\text{comp}} \leq 0 \tag{A204}$$

$$\gamma^{0,\text{comp}} + \gamma^{1,\text{comp}} + \gamma^{2,\text{comp}} + \gamma^{3,\text{comp}} + \gamma^{4,\text{comp}} = \gamma^{\text{op,comp}} \tag{A205}$$

$$\begin{aligned} p^{\text{comp}} = {} & a_{52}^{\text{comp}} \cdot \gamma^{4,\text{comp}} + a_{53}^{\text{comp}} \cdot \gamma^{1,\text{comp}} + \\ & a_{54}^{\text{comp}} \cdot \gamma^{2,\text{comp}} + a_{55}^{\text{comp}} \cdot x_1^{0,\text{comp}} + a_{56}^{\text{comp}} \cdot x_2^{4,\text{comp}} + \\ & a_{57}^{\text{comp}} \cdot x_1^{1,\text{comp}} + a_{58}^{\text{comp}} \cdot x_2^{1,\text{comp}} + a_{59}^{\text{comp}} \cdot x_1^{3,\text{comp}} + \\ & a_{60}^{\text{comp}} \cdot x_1^{4,\text{comp}} + a_{61}^{\text{comp}} \cdot x_1^{2,\text{comp}} + a_{62}^{\text{comp}} \cdot x_2^{2,\text{comp}} + \\ & a_{63}^{\text{comp}} \cdot x_2^{3,\text{comp}} + a_{64}^{\text{comp}} \cdot x_2^{0,\text{comp}} + a_{65}^{\text{comp}} \cdot \gamma^{3,\text{comp}} + \\ & a_{66}^{\text{comp}} \cdot \gamma^{0,\text{comp}} + a_{67}^{\text{comp}} \cdot x_0^{0,\text{comp}} + a_{68}^{\text{comp}} \cdot x_0^{1,\text{comp}} + \\ & a_{69}^{\text{comp}} \cdot x_0^{4,\text{comp}} + a_{70}^{\text{comp}} \cdot x_0^{3,\text{comp}} + a_{71}^{\text{comp}} \cdot x_0^{2,\text{comp}} \end{aligned} \tag{A206}$$

$$\epsilon pr^{\text{comp,in}} = x_0^{0,\text{comp}} + x_0^{1,\text{comp}} + x_0^{2,\text{comp}} + x_0^{3,\text{comp}} + x_0^{4,\text{comp}} \tag{A207}$$

$$\epsilon pr^{\text{comp,out}} = x_1^{0,\text{comp}} + x_1^{1,\text{comp}} + x_1^{2,\text{comp}} + x_1^{3,\text{comp}} + x_1^{4,\text{comp}} \tag{A208}$$

$$n^{\text{H2,comp}} = x_2^{0,\text{comp}} + x_2^{1,\text{comp}} + x_2^{2,\text{comp}} + x_2^{3,\text{comp}} + x_2^{4,\text{comp}} \tag{A209}$$

Table A6. Constants for the piecewise linear model of the compressor.

Constant	Value	Constant	Value	Constant	Value
a_0^{comp}	0.0124	a_1^{comp}	−1.00	a_2^{comp}	8.00
a_3^{comp}	−7.00	a_4^{comp}	−0.0619	a_5^{comp}	−120.
a_6^{comp}	2.00	a_7^{comp}	5.56	a_8^{comp}	120.0
a_9^{comp}	0.0619	a_{10}^{comp}	7.00	a_{11}^{comp}	120.0
a_{12}^{comp}	0.0619	a_{13}^{comp}	7.00	a_{14}^{comp}	89.6
a_{15}^{comp}	6.55	a_{16}^{comp}	89.3	a_{17}^{comp}	0.0619

Table A6. *Cont.*

Constant	Value	Constant	Value	Constant	Value
a_{18}^{comp}	5.40	a_{19}^{comp}	42.3	a_{20}^{comp}	0.0317
a_{21}^{comp}	0.0704	a_{22}^{comp}	−0.00117	a_{23}^{comp}	−4.58
a_{24}^{comp}	0.00325	a_{25}^{comp}	6.06	a_{26}^{comp}	−0.0360
a_{27}^{comp}	−0.00404	a_{28}^{comp}	0.00117	a_{29}^{comp}	4.58
a_{30}^{comp}	−0.0317	a_{31}^{comp}	−0.0704	a_{32}^{comp}	0.00104
a_{33}^{comp}	3.78	a_{34}^{comp}	−0.00841	a_{35}^{comp}	−0.0487
a_{36}^{comp}	0.0360	a_{37}^{comp}	0.00404	a_{38}^{comp}	−0.00325
a_{39}^{comp}	−6.06	a_{40}^{comp}	4.09	a_{41}^{comp}	−0.00857
a_{42}^{comp}	−0.0101	a_{43}^{comp}	−0.00532	a_{44}^{comp}	0.00841
a_{45}^{comp}	0.0487	a_{46}^{comp}	−0.00104	a_{47}^{comp}	−3.78
a_{48}^{comp}	0.00857	a_{49}^{comp}	0.0101	a_{50}^{comp}	0.00532
a_{51}^{comp}	−4.09	a_{52}^{comp}	0.00108	a_{53}^{comp}	0.000534
a_{54}^{comp}	0.0147	a_{55}^{comp}	0.00258	a_{56}^{comp}	5.14
a_{57}^{comp}	0.00145	a_{58}^{comp}	9.25	a_{59}^{comp}	0.00469
a_{60}^{comp}	0.0103	a_{61}^{comp}	0.00523	a_{62}^{comp}	3.45
a_{63}^{comp}	9.28	a_{64}^{comp}	13.8	a_{65}^{comp}	−0.00710
a_{66}^{comp}	−0.0305	a_{67}^{comp}	−0.0898	a_{68}^{comp}	−0.0235
a_{69}^{comp}	−0.0621	a_{70}^{comp}	−0.0727	a_{71}^{comp}	−0.0218

Appendix A.7. Electrolyzer Power Simplified

$$x_0^{\text{ey,simp}} \leq a_0^{\text{ey,simp}} \cdot \gamma^{0,\text{ey,simp}} \tag{A210}$$

$$x_0^{\text{ey,simp}} \geq a_1^{\text{ey,simp}} \cdot \gamma^{0,\text{ey,simp}} \tag{A211}$$

$$x_1^{\text{ey,simp}} \leq a_2^{\text{ey,simp}} \cdot \gamma^{1,\text{ey,simp}} \tag{A212}$$

$$x_1^{\text{ey,simp}} \geq a_0^{\text{ey,simp}} \cdot \gamma^{1,\text{ey,simp}} \tag{A213}$$

$$x_0^{\text{ey,simp}} + x_1^{\text{ey,simp}} = p^{\text{ey}} \tag{A214}$$

$$a_3^{\text{ey,simp}} \cdot \gamma^{1,\text{ey,simp}} + a_4^{\text{ey,simp}} \cdot \gamma^{0,\text{ey,simp}} + a_5^{\text{ey,simp}} \cdot x_1^{\text{ey,simp}} + a_6^{\text{ey,simp}} \cdot x_0^{\text{ey,simp}} = n^{\text{H2,ey}} \tag{A215}$$

$$\gamma^{0,\text{ey,simp}} + \gamma^{1,\text{ey,simp}} = \gamma^{\text{op,ey}} \tag{A216}$$

Table A7. Constants for the simplified piecewise linear model of the power output of the electrolyzer.

Constant	Value	Constant	Value	Constant	Value
$a_0^{\text{ey,simp}}$	15.6	$a_1^{\text{ey,simp}}$	4.85	$a_2^{\text{ey,simp}}$	34.1
$a_3^{\text{ey,simp}}$	0.00446	$a_4^{\text{ey,simp}}$	0.00166	$a_5^{\text{ey,simp}}$	0.00230
$a_6^{\text{ey,simp}}$	0.00248				

Appendix A.8. Fuel Cell Power Simplified

$$x_0^{\mathrm{fc,simp}} \leq a_0^{\mathrm{fc,simp}} \cdot \gamma^{0,\mathrm{fc,simp}} \tag{A217}$$

$$x_0^{\mathrm{fc,simp}} \geq a_1^{\mathrm{fc,simp}} \cdot \gamma^{0,\mathrm{fc,simp}} \tag{A218}$$

$$x_1^{\mathrm{fc,simp}} \leq a_2^{\mathrm{fc,simp}} \cdot \gamma^{1,\mathrm{fc,simp}} \tag{A219}$$

$$x_1^{\mathrm{fc,simp}} \geq a_0^{\mathrm{fc,simp}} \cdot \gamma^{1,\mathrm{fc,simp}} \tag{A220}$$

$$x_2^{\mathrm{fc,simp}} \leq a_3^{\mathrm{fc,simp}} \cdot \gamma^{2,\mathrm{fc,simp}} \tag{A221}$$

$$x_2^{\mathrm{fc,simp}} \geq a_2^{\mathrm{fc,simp}} \cdot \gamma^{2,\mathrm{fc,simp}} \tag{A222}$$

$$x_3^{\mathrm{fc,simp}} \leq a_4^{\mathrm{fc,simp}} \cdot \gamma^{3,\mathrm{fc,simp}} \tag{A223}$$

$$x_3^{\mathrm{fc,simp}} \geq a_3^{\mathrm{fc,simp}} \cdot \gamma^{3,\mathrm{fc,simp}} \tag{A224}$$

$$x_4^{\mathrm{fc,simp}} \leq a_5^{\mathrm{fc,simp}} \cdot \gamma^{4,\mathrm{fc,simp}} \tag{A225}$$

$$x_4^{\mathrm{fc,simp}} \geq a_4^{\mathrm{fc,simp}} \cdot \gamma^{4,\mathrm{fc,simp}} \tag{A226}$$

$$x_0^{\mathrm{fc,simp}} + x_1^{\mathrm{fc,simp}} + x_2^{\mathrm{fc,simp}} + x_3^{\mathrm{fc,simp}} + x_4^{\mathrm{fc,simp}} = p^{\mathrm{fc}} \tag{A227}$$

$$\begin{aligned} a_{10}^{\mathrm{fc,simp}} \cdot x_3^{\mathrm{fc,simp}} + a_{11}^{\mathrm{fc,simp}} \cdot \gamma^{3,\mathrm{fc,simp}} + a_{12}^{\mathrm{fc,simp}} \cdot \gamma^{1,\mathrm{fc,simp}} \\ + a_{13}^{\mathrm{fc,simp}} \cdot \gamma^{2,\mathrm{fc,simp}} + a_{14}^{\mathrm{fc,simp}} \cdot \gamma^{0,\mathrm{fc,simp}} + a_{15}^{\mathrm{fc,simp}} \cdot \gamma^{4,\mathrm{fc,simp}} + a_6^{\mathrm{fc,simp}} \cdot x_1^{\mathrm{fc,simp}} \\ + a_7^{\mathrm{fc,simp}} \cdot x_2^{\mathrm{fc,simp}} + a_8^{\mathrm{fc,simp}} \cdot x_4^{\mathrm{fc,simp}} + a_9^{\mathrm{fc,simp}} \cdot x_0^{\mathrm{fc,simp}} = n^{\mathrm{H2,fc}} \end{aligned} \tag{A228}$$

$$\gamma^{0,\mathrm{fc,simp}} + \gamma^{1,\mathrm{fc,simp}} + \gamma^{2,\mathrm{fc,simp}} + \gamma^{3,\mathrm{fc,simp}} + \gamma^{4,\mathrm{fc,simp}} = \gamma^{\mathrm{op,fc}} \tag{A229}$$

Table A8. Constants for the simplified piecewise linear model of the power output of the fuel cell.

Constant	Value	Constant	Value	Constant	Value
$a_0^{\mathrm{fc,simp}}$	2.21	$a_1^{\mathrm{fc,simp}}$	0.827	$a_2^{\mathrm{fc,simp}}$	3.32
$a_3^{\mathrm{fc,simp}}$	4.14	$a_4^{\mathrm{fc,simp}}$	4.71	$a_5^{\mathrm{fc,simp}}$	5.23
$a_6^{\mathrm{fc,simp}}$	0.00964	$a_7^{\mathrm{fc,simp}}$	0.0121	$a_8^{\mathrm{fc,simp}}$	0.0206
$a_9^{\mathrm{fc,simp}}$	0.00784	$a_{10}^{\mathrm{fc,simp}}$	0.0155	$a_{11}^{\mathrm{fc,simp}}$	−0.0273
$a_{12}^{\mathrm{fc,simp}}$	−0.00515	$a_{13}^{\mathrm{fc,simp}}$	−0.0132	$a_{14}^{\mathrm{fc,simp}}$	−0.00117
$a_{15}^{\mathrm{fc,simp}}$	−0.0516				

References

1. Umweltbundesamt. *Erneuerbare Energien in Deutschland 2020: Daten zur Entwicklung im Jahr 2020*; Umweltbundesamt: Dessau-Roßlau, Germany, 2021.
2. Marocco, P.; Ferrero, D.; Martelli, E.; Santarelli, M.; Lanzini, A. An MILP approach for the optimal design of renewable battery-hydrogen energy systems for off-grid insular communities. *Energy Convers. Manag.* **2021**, *245*, 114564. [CrossRef]
3. Le, T.S.; Nguyen, T.N.; Bui, D.K.; Ngo, T.D. Optimal sizing of renewable energy storage: A techno-economic analysis of hydrogen, battery and hybrid systems considering degradation and seasonal storage. *Appl. Energy* **2023**, *336*, 120817. [CrossRef]
4. Ulleberg, Ø. *Stand-Alone Power Systems for the Future: Optimal Design, Operation and Control of Solar-Hydrogen Energy Systems*; Operation & Control of Solar-Hydrogen Energy Systems: Trondheim, Norway, 1998.
5. Gabrielli, P.; Gazzani, M.; Martelli, E.; Mazzotti, M. Optimal design of multi-energy systems with seasonal storage. *Appl. Energy* **2018**, *219*, 408–424. [CrossRef]
6. Kotzur, L.; Markewitz, P.; Robinius, M.; Stolten, D. Time series aggregation for energy system design: Modeling seasonal storage. *Appl. Energy* **2018**, *213*, 123–135. [CrossRef]

7. Petkov, I.; Gabrielli, P. Power-to-hydrogen as seasonal energy storage: An uncertainty analysis for optimal design of low-carbon multi-energy systems. *Appl. Energy* **2020**, *274*, 115197. [CrossRef]
8. Marocco, P.; Ferrero, D.; Lanzini, A.; Santarelli, M. The role of hydrogen in the optimal design of off-grid hybrid renewable energy systems. *J. Energy Storage* **2022**, *46*, 103893. [CrossRef]
9. Chauhan, A.; Saini, R.P. A review on Integrated Renewable Energy System based power generation for stand-alone applications: Configurations, storage options, sizing methodologies and control. *Renew. Sustain. Energy Rev.* **2014**, *38*, 99–120. [CrossRef]
10. Ipsakis, D.; Voutetakis, S.; Seferlis, P.; Stergiopoulos, F.; Elmasides, C. Power management strategies for a stand-alone power system using renewable energy sources and hydrogen storage. *Int. J. Hydrogen Energy* **2009**, *34*, 7081–7095. [CrossRef]
11. Olatomiwa, L.; Mekhilef, S.; Ismail, M.S.; Moghavvemi, M. Energy management strategies in hybrid renewable energy systems: A review. *Renew. Sustain. Energy Rev.* **2016**, *62*, 821–835. [CrossRef]
12. Modu, B.; Abdullah, M.P.; Bukar, A.L.; Hamza, M.F. A systematic review of hybrid renewable energy systems with hydrogen storage: Sizing, optimization, and energy management strategy. *Int. J. Hydrogen Energy* **2023**, *48*, 38354–38373. [CrossRef]
13. Bordons, C.; Garcia-Torres, F.; Ridao, M.A. *Model Predictive Control of Microgrids*; Springer: Berlin/Heidelberg, Germany, 2020; Volume 358. [CrossRef]
14. Modu, B.; Abdullah, M.P.; Bukar, A.L.; Hamza, M.F.; Adewolu, M.S. Energy management and capacity planning of photovoltaic-wind-biomass energy system considering hydrogen-battery storage. *J. Energy Storage* **2023**, *73*, 109294. [CrossRef]
15. Li, Z.; Liu, Y.; Du, M.; Cheng, Y.; Shi, L. Modeling and multi-objective optimization of a stand-alone photovoltaic-wind turbine-hydrogen-battery hybrid energy system based on hysteresis band. *Int. J. Hydrogen Energy* **2023**, *48*, 7959–7974. [CrossRef]
16. Alili, H.; Mahmoudimehr, J. Techno-economic assessment of integrating hydrogen energy storage technology with hybrid photovoltaic/pumped storage hydropower energy system. *Energy Convers. Manag.* **2023**, *294*, 117437. [CrossRef]
17. Garcia-Torres, F.; Valverde, L.; Bordons, C. Optimal Load Sharing of Hydrogen-Based Microgrids With Hybrid Storage Using Model-Predictive Control. *IEEE Trans. Ind. Electron.* **2016**, *63*, 4919–4928. [CrossRef]
18. Valverde, L.; Bordons, C.; Rosa, F. Integration of Fuel Cell Technologies in Renewable-Energy-Based Microgrids Optimizing Operational Costs and Durability. *IEEE Trans. Ind. Electron.* **2016**, *63*, 167–177. [CrossRef]
19. Garcia-Torres, F.; Bordons, C. Optimal Economical Schedule of Hydrogen-Based Microgrids With Hybrid Storage Using Model Predictive Control. *IEEE Trans. Ind. Electron.* **2015**, *62*, 5195–5207. [CrossRef]
20. Cau, G.; Cocco, D.; Petrollese, M.; Knudsen Kær, S.; Milan, C. Energy management strategy based on short-term generation scheduling for a renewable microgrid using a hydrogen storage system. *Energy Convers. Manag.* **2014**, *87*, 820–831. [CrossRef]
21. Fan, F.; Zhang, R.; Xu, Y. Robustly coordinated operation of an emission-free microgrid with hybrid hydrogen-battery energy storage. *CSEE J. Power Energy Syst.* **2021**, *8*, 369–379. [CrossRef]
22. Li, Q.; Qiu, Y.; Yang, H.; Xu, Y.; Chen, W.; Wang, P. Stability-constrained two-stage robust optimization for integrated hydrogen hybrid energy system. *CSEE J. Power Energy Syst.* **2020**, *7*, 162–171. [CrossRef]
23. Cardona, P.; Costa-Castelló, R.; Roda, V.; Carroquino, J.; Valiño, L.; Serra, M. Model predictive control of an on-site green hydrogen production and refuelling station. *Int. J. Hydrogen Energy* **2023**, *48*, 17995–18010. [CrossRef]
24. Gonzalez-Rivera, E.; Garcia-Trivino, P.; Sarrias-Mena, R.; Torreglosa, J.P.; Jurado, F.; Fernandez-Ramirez, L.M. Model Predictive Control-Based Optimized Operation of a Hybrid Charging Station for Electric Vehicles. *IEEE Access* **2021**, *9*, 115766–115776. [CrossRef]
25. Yassuda Yamashita, D.; Vechiu, I.; Gaubert, J.P. Two-level hierarchical model predictive control with an optimised cost function for energy management in building microgrids. *Appl. Energy* **2021**, *285*, 116420. [CrossRef]
26. Thaler, B.; Posch, S.; Wimmer, A.; Pirker, G. Hybrid model predictive control of renewable microgrids and seasonal hydrogen storage. *Int. J. Hydrogen Energy* **2023**, *161*, 48. [CrossRef]
27. Neisen, V.; Baader, F.J.; Abel, D. Supervisory Model-based Control using Mixed Integer Optimization for stationary hybrid fuel cell systems. *IFAC-PapersOnLine* **2018**, *51*, 320–325. [CrossRef]
28. Weimann, L.; Gabrielli, P.; Boldrini, A.; Kramer, G.J.; Gazzani, M. Optimal hydrogen production in a wind-dominated zero-emission energy system. *Adv. Appl. Energy* **2021**, *3*, 100032. [CrossRef]
29. Yassuda Yamashita, D.; Vechiu, I.; Gaubert, J.P.; Jupin, S. Autonomous observer of hydrogen storage to enhance a model predictive control structure for building microgrids. *J. Energy Storage* **2022**, *53*, 105072. [CrossRef]
30. Huang, C.; Zong, Y.; You, S.; Træholt, C. Economic model predictive control for multi-energy system considering hydrogen-thermal-electric dynamics and waste heat recovery of MW-level alkaline electrolyzer. *Energy Convers. Manag.* **2022**, *265*, 115697. [CrossRef]
31. Abdelghany, M.B.; Al-Durra, A.; Zeineldin, H.; Hu, J. Integration of cascaded coordinated rolling horizon control for output power smoothing in islanded wind–solar microgrid with multiple hydrogen storage tanks. *Energy* **2024**, *291*, 130442. [CrossRef]
32. Abdelghany, M.B.; Al-Durra, A.; Daming, Z.; Gao, F. Optimal multi-layer economical schedule for coordinated multiple mode operation of wind–solar microgrids with hybrid energy storage systems. *J. Power Sources* **2024**, *591*, 233844. [CrossRef]
33. Li, Z.; Xia, Y.; Bo, Y.; Wei, W. Optimal planning for electricity-hydrogen integrated energy system considering multiple timescale operations and representative time-period selection. *Appl. Energy* **2024**, *362*, 122965. [CrossRef]
34. Birkelbach, F.; Huber, D.; Hofmann, R. Piecewise linear approximation for MILP leveraging piecewise convexity to improve performance. *Comput. Chem. Eng.* **2024**, *183*, 108596. [CrossRef]

35. Neisen, V.; Futing, M.; Abel, D. Optimization Approaches for Model Predictive Power Flow Control in Hybrid Fuel Cell Systems. In Proceedings of the IECON 2019—45th Annual Conference of the IEEE Industrial Electronics Society, Lisbon, Portugal, 14–17 October 2019; IEEE: Piscataway, NJ, USA, 2019; pp. 4575–4582. [CrossRef]
36. Ulleberg, Ø. Modeling of advanced alkaline electrolyzers: A system simulation approach. *Int. J. Hydrogen Energy* **2003**, *28*, 21–33. [CrossRef]
37. Li, B.; Miao, H.; Li, J. Multiple hydrogen-based hybrid storage systems operation for microgrids: A combined TOPSIS and model predictive control methodology. *Appl. Energy* **2021**, *283*, 116303. [CrossRef]
38. Khaligh, V.; Ghezelbash, A.; Zarei, M.; Liu, J.; Won, W. Efficient integration of alkaline water electrolyzer – A model predictive control approach for a sustainable low-carbon district heating system. *Energy Convers. Manag.* **2023**, *292*, 117404. [CrossRef]
39. Pan, G.; Gu, W.; Lu, Y.; Qiu, H.; Lu, S.; Yao, S. Optimal Planning for Electricity-Hydrogen Integrated Energy System Considering Power to Hydrogen and Heat and Seasonal Storage. *IEEE Trans. Sustain. Energy* **2020**, *11*, 2662–2676. [CrossRef]
40. Kämper, A.; Holtwerth, A.; Leenders, L.; Bardow, A. AutoMoG 3D: Automated Data-Driven Model Generation of Multi-Energy Systems Using Hinging Hyperplanes. *Front. Energy Res.* **2021**, *9*, 719658. [CrossRef]
41. Holtwerth, A.; Xhonneux, A.; Muller, D. Data-Driven Generation of Mixed-Integer Linear Programming Formulations for Model Predictive Control of Hybrid Energy Storage Systems using detailed nonlinear Simulation Models. In Proceedings of the 2022 Open Source Modelling and Simulation of Energy Systems (OSMSES), Aachen, Germany, 4–5 April 2022; IEEE: Piscataway, NJ, USA, 2022; pp. 1–6. [CrossRef]
42. Holtwerth, A. LinMoG: Linear Model Generation. 2024. Available online: https://jugit.fz-juelich.de/iek-10/public/optimization/linmog (accessed on 15 January 2024).
43. Wakui, T.; Akai, K.; Yokoyama, R. Shrinking and receding horizon approaches for long-term operational planning of energy storage and supply systems. *Energy* **2022**, *239*, 122066. [CrossRef]
44. Guo, Z.; Wei, W.; Bai, J.; Mei, S. Long-term operation of isolated microgrids with renewables and hybrid seasonal-battery storage. *Appl. Energy* **2023**, *349*, 121628. [CrossRef]
45. Abdelghany, M.B.; Shehzad, M.F.; Liuzza, D.; Mariani, V.; Glielmo, L. Optimal operations for hydrogen-based energy storage systems in wind farms via model predictive control. *Int. J. Hydrogen Energy* **2021**, *46*, 29297–29313. [CrossRef]
46. Abdelghany, M.B.; Al-Durra, A.; Zeineldin, H.; Gao, F. Integrating scenario-based stochastic-model predictive control and load forecasting for energy management of grid-connected hybrid energy storage systems. *Int. J. Hydrogen Energy* **2023**, *48*, 35624–35638. [CrossRef]
47. Abdelghany, M.B.; Mariani, V.; Liuzza, D.; Glielmo, L. Hierarchical model predictive control for islanded and grid-connected microgrids with wind generation and hydrogen energy storage systems. *Int. J. Hydrogen Energy* **2024**, *51*, 595–610. [CrossRef]
48. Holtwerth, A.; Xhonneux, A.; Müller, D. Closed Loop Model Predictive Control of a Hybrid Battery-Hydrogen Energy Storage System using Mixed-Integer Linear Programming. *Energy Convers. Manag. X* **2024**, *22*, 100561. [CrossRef]
49. Barthels, H.; Brocke, W.A.; Bonhoff, K.; Groehn, H.G.; Heuts, G.; Lennartz, M.; Mai, H.; Mergel, J.; Schmid, L.; Ritzenhoff, P. Phoebus-Jülich: An autonomous energy supply system comprising photovoltaics, electrolytic hydrogen, fuel cell. *Int. J. Hydrogen Energy* **1998**, *23*, 295–301. [CrossRef]
50. Barthels, H. *PHOEBUS—Das Jülicher System Photovoltaik-Elektrolyse-Brennstoffzelle*; Springer: Berlin/Heidelberg, Germany, 1996.
51. Meurer, C.; Barthels, H.; Brocke, W.A.; Emonts, B.; Groehn, H.G. PHOEBUS—An autonomous supply system with renewable energy: Six years of operational experience and advanced concepts. *Sol. Energy* **1999**, *67*, 131–138. [CrossRef]
52. Ghosh, P.; Emonts, B.; Janßen, H.; Mergel, J.; Stolten, D. Ten years of operational experience with a hydrogen-based renewable energy supply system. *Sol. Energy* **2003**, *75*, 469–478. [CrossRef]
53. Langiu, M.; Shu, D.Y.; Baader, F.J.; Hering, D.; Bau, U.; Xhonneux, A.; Müller, D.; Bardow, A.; Mitsos, A.; Dahmen, M. COMANDO: A Next-Generation Open-Source Framework for Energy Systems Optimization. *Comput. Chem. Eng.* **2021**, *152*, 107366. [CrossRef]
54. Gurobi Optimization LLC. *Gurobi Optimizer Reference Manual*; Gurobi Optimization LLC: Beaverton, OR, USA, 2022.

Disclaimer/Publisher's Note: The statements, opinions and data contained in all publications are solely those of the individual author(s) and contributor(s) and not of MDPI and/or the editor(s). MDPI and/or the editor(s) disclaim responsibility for any injury to people or property resulting from any ideas, methods, instructions or products referred to in the content.